CHAPTER

# DIELECTRIC PROPERTIES OF $Y_{2/3}Cu_3Ti_{4-x}Fe_xO_{12}$ (x = 0.0.5, 0.10, 0.15 and 0.20) SYNTHESIZED BY SEMI-WET ROUTE

6

## 6.1 INTRODUCTION

Due to high demand and rapid progress in miniaturization of electrical components, considerable attention has been paid to the role as well as function of small size high dielectric constant (ε) materials. A great challenge in microelectronics is to decrease the size of passive components, in general, and capacitors in particular. The high ε ceramics make it possible to miniaturize the passive microwave devices. Their size can typically be reduced in comparison to classical resonators and filters by a factor of $1/\sqrt{\varepsilon}$. For these reasons, the last decade had witnessed potential interest in the study of the giant dielectric permittivity of the complex cubic perovskites. Many research papers on high dielectric constant materials are available in literature since the stunning discovery of $ACu_3Ti_4O_{12}$ (A = Ca, $Bi_{2/3}$, $Y_{2/3}$, $La_{2/3}$, $Gd_{2/3}$) type perovskite (Homes *et al.*, 2001; Liu *et al.*, 2005). The correlation between the crystal structure and intrinsic dielectric properties of a cubic perovskite-related family of compounds such as $ACu_3Ti_4O_{12}$ has been a controversial issue for several years, especially for $CaCu_3Ti_4O_{12}$ (CCTO), the most studied member of this family The devastating discovery of high-dielectric-constant in $CaCu_3Ti_4O_{12}$ type perovskite has raised considerable interest for various research groups, especially those of Homes *et al.* (2001); Subramanian *et al.* (2002) and Hongtao *et al.* (2007). CCTO possesses a distorted complex perovskite structure with the space group $Im_3$ and has lattice parameter of 7.391 Å. Dielectric behaviour of calcium copper titanate exhibits an extraordinary high dielectric constant $\varepsilon \sim 10^4$ - $10^5$ and shows good thermal stability in a wide temperature range, 100 to 600K, was first discovered by Subramanian et al. in 2000. Such type of temperature independent behavior of CCTO is technically appealing alternative for the currently used ferroelectric materials and for the

development of future microelectronic devices. At the same time it has a potential for technological applications in capacitive components and memory devices specifically in dynamic random access memory (DRAMs) due to the possibility to reduce the dimensions needed in microelectronic equipments (Hongtao *et al*., 2000). But CCTO is not the whole one but any transition metal titanate can equally meet these features. Rather other metal titanate containing a inner-transition metal cations such as $Nd_{2/3}$, $Sm_{2/3}$, $Gd_{2/3}$, $Dy_{2/3}$ at the place of Ca cation also exhibit high dielectric constant with good thermal stability (Liu *et al.*, 2005). One of the materials, $Y_{2/3}Cu_3Ti_4O_{12}$ (YCTO) is structurally analogous to $CaCu_3Ti_4O_{12}$ (CCTO) ceramic. At present, very few works have been reported on YCTO. An undoped YCTO nano-sized material, prepared by the semi-wet route, exhibits high dielectric constant (ε ~8,434) at room temperature and at 100 Hz. However, the most challenging factor is its dielectric loss. Undoped YCTO shows a quite high dielectric loss (tan δ~1.5-2.04) in the temperature range 308-428 K, which needs further improvement within the acceptable ranges for device applications(Adams *et al.*, 2006). It is reported in the literature that the partial isovalent substitution of metal cations at different sites of perovskite can improve properties associated with ferroelectricity and dielectric response in ceramic. Further, structural flexibility and chemical versatility of the materials make them more suitable for device applications (Li *et al.*, 2008, Rai *et al*., 2009). The only property, which restricts the broad applications of this YCTO ceramic, is its high dielectric loss and in the present chapter, an attempt has been made to minimize the tangent loss (tan δ) by using the semi-wet route for the synthesis of the ceramic.

Regarding above importance and unavailability of experimental data on the YCTO material, we have worked out a methodology to control its dielectric loss factor by doping of $Fe^{3+}$ at $Ti^{4+}$-site of YCTO. In this chapter a few samples of the system $Y_{2/3}Cu_3Ti_{4-x}Fe_xO_{12}$ ($x$ = 0.00, 0.05, 0.10, 0.15 and 0.20) abbreviated as YCTFO were synthesized by the semi-wet route and its dielectric properties are reported. These samples are characterized by powder X-ray diffraction (XRD), Scanning electron microscopy (SEM), energy dispersive X-ray spectroscopy (EDX), transmission electron microscopy (TEM) and atomic force microscopy (AFM). A comparative study of the dielectric properties of YCTFO systems with YCTO was also illustrated in this chapter.

## 6.2 RESULTS AND DISCUSSION

### 6.2.1 Thermal Analysis

The ideal temperature required for the thermal decomposition of precursor dry powder of $Y_{2/3}Cu_3Ti_{4-x}Fe_xO_{12}$ ($x$ = 0.10), as a representative ceramic, was ascertained using TG/DTA. Fig. 6.1 shows simultaneous TG/DTA/DTG plots of dry precursor powder of $Y_{2/3}Cu_3Ti_{4-x}Fe_xO_{12}$ ceramic ($x$ = 0.10). Two major stages of weight loss in the temperature range from 100 to 1000 $x$ was observed in TGA plot, the first major weight loss at 230 $^{\circ}$C is due to dehydration and combustion of the gel while the second weight loss at 850 $^{\circ}$C is due to the formation of an intermediate compound.

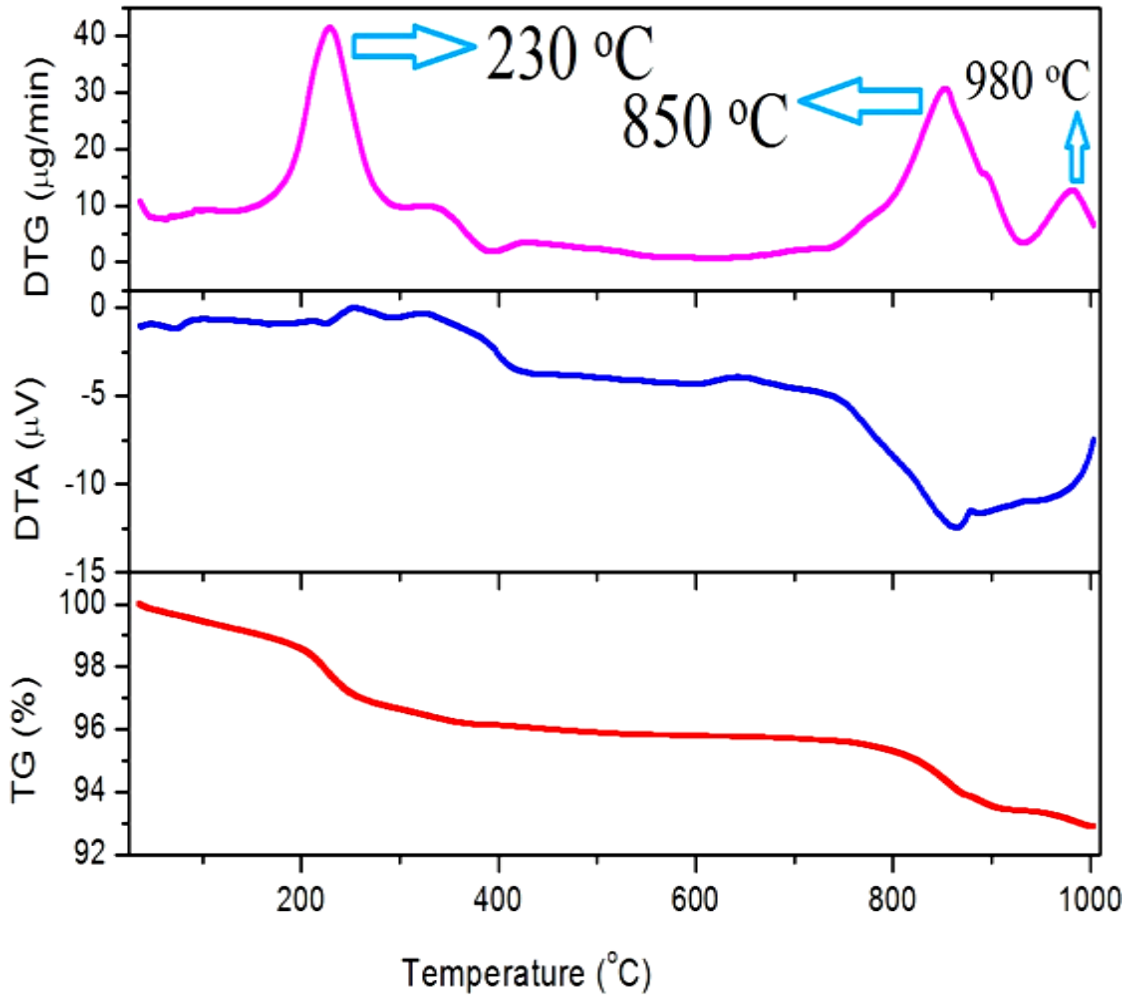


Figure 6.1: TG/DTA/DTG plots of precursor dry powder of $Y_{2/3}Cu_3Ti_{4-x}Fe_xO_{12}$ ($x$ = 0.10) ceramic.

Further, an additional but slight weight loss at 980 °C was also observed which is due to an exothermic addition reaction of the intermediate compound to give the final product $Y_{2/3}Cu_3Ti_{4-x}Fe_xO_{12}$ ($x$ = 0.10). The corresponding DTA and DTG plot also show two strong exothermic peaks near 230 °C and 850 °C besides a small peak at 980 °C. It was also observed that DTG peaks are more intense than DTA peaks.

## 6.2.2 X-Ray Diffraction Analysis

XRD patterns of different iron doped YCTO i.e. $Y_{2/3}Cu_3Ti_{4-x}Fe_xO_{12}$ with $x$ = 0.05, 0.10, 0.15 and 0.20 ceramic sintered at 1000 °C for 12 h is illustrated in Fig. 6.2. The peaks obtained were indexed on the basis of a cubic unit cell similar to undoped $CaCu_3Ti_4O_{12}$. All samples show distinct peaks corresponding to (211), (220), (30), (222), (321), (400), (422) and (440) orientations. These peaks are in a good agreement with $CaCu_3Ti_4O_{12}$ (JCPDS card no. 75-2188), demonstrating a polycrystalline characteristic of YCTFO ceramic. In addition to the major phase YCTFO some minor phase of CuO (JCPDS 80-1917) was also observed in the figure. The XRD pattern of the sample with $x$ = 0.05-0.20 were almost identical with that of $x$ = 0.00 and at the same time, not a single Fe-related phase was detected indicating higher solubility of Fe in the YCTO ceramic.

The lattice parameter and unit cell volume of YCTFO ceramic was calculated using the Cel software is listed in the Table 6.1. It is also evident from Table 6.1 that the lattice constant increases monotonically with increase in $x$ value. It indicates that the $Fe^{3+}$ may have taken the place of $Ti^{4+}$ as expected. The increase of the lattice constant with doping concentration may be due to larger ionic radii of the dopant $Fe^{3+}$ (0.785Å) to that of parent $Ti^{4+}$ (0.745Å).

The presence of split peaks in XRD pattern for the reflections 400, 422 and 440 may be due to the presence of Cu-K$\alpha_2$ along with Cu-K$\alpha_1$ in the X-ray radiation used for diffraction. It is supported by the fact that in all these reflections, the intensity of peaks due to Cu-K$\alpha_2$ is close to 50% of the intensity of peak due to Cu K$\alpha_1$ as expected (Culity *et al*., 2001).

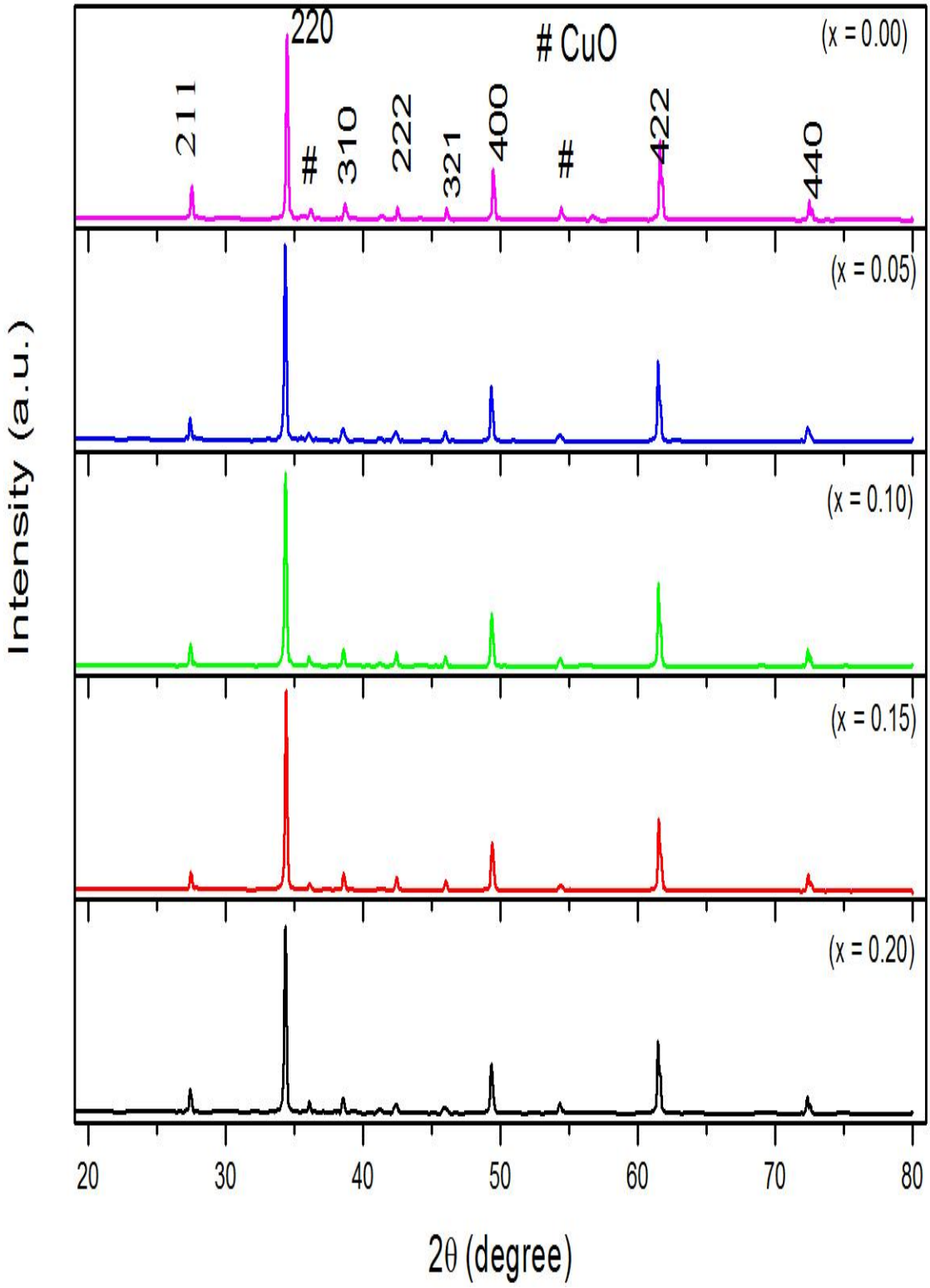


Figure 6.2: Powder X-ray diffraction patterns of $Y_{2/3}Cu_3Ti_{4-x}Fe_xO_{12}$ ($x$ = 0.00, 0.05, 0.10, 0.15 and 0.20) sintered at 1000 $^{\circ}$C for 12h.

The crystallite size (D) of the different YCTFO ceramic were estimated using the Debye-Scherrer's formula, shown in equation (6.1)

$$D = \frac{k\lambda}{\beta \cos\theta} \tag{6.1}$$

where k is the crystal shape coefficient (k = 0.89), λ is the wave length of X-ray radiation, θ is the diffraction angle and β is the corrected full width at half maximum (FWHM) obtained after correcting the peak broadening due to instrument. It is reported earlier that XRD peaks get broadened due to the instrument and lattice defects (Delhez *et al*., 1982). For correction in peak broadening a few main peaks with greater intensity within the XRD pattern were selected for $Y_{2/3}Cu_3Ti_{4-x}Fe_xO_{12}$ ($x$ = 0.10) sample. The silicon wafer was taken as a reference material to determine the peak broadening due to instrument. Knowing the slope and intercept of the straight line obtained by Williamson-Hall Plot (Fig. 6.3), lattice strain and the actual crystallite size (D) for the sample $x$ = 0. 10 were determined to be 0.36% and 6.809 nm respectively. The calculated value of crystallite size, after correction in the instrumental broadening for different $Y_{2/3}Cu_3Ti_{4-x}Fe_xO_{12}$ ($x$ = 0. 00, 0.10, 0.15 and 0.20) ceramics are also shown in Table 6.1. These are also in the nano-particle range.

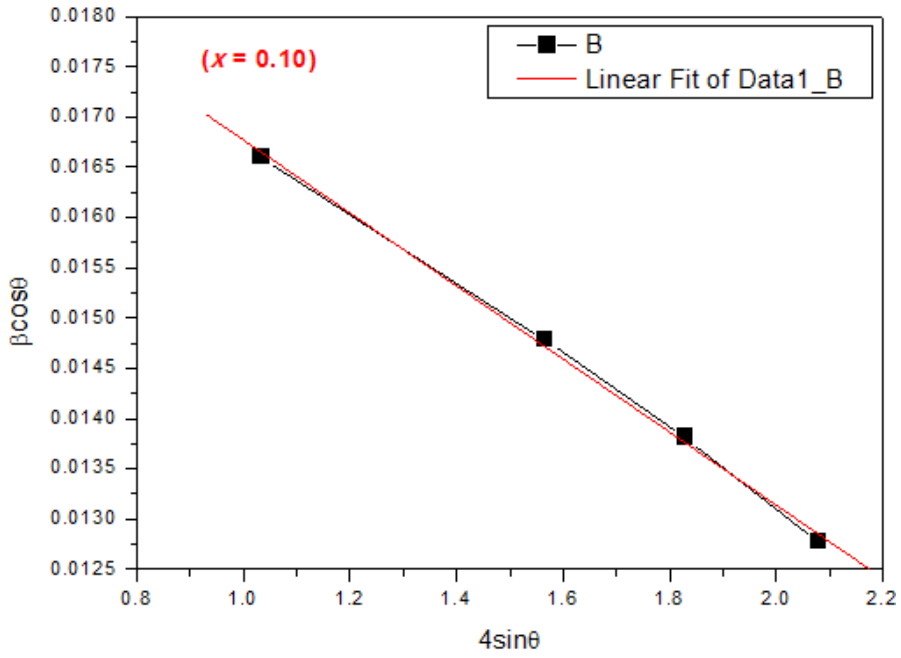


Figure 6.3: Williamson-Hall Plot for sintered $Y_{2/3}Cu_3Ti_{4-x}Fe_xO_{12}$ ($x$ = 0.10) ceramic.

**Table 6.1:** Crystal structure, lattice parameter and unit cell volume of $Y_{2/3}Cu_3Ti_{4-x}Fe_xO_{12}$ ($x$ = 0.00, 0.05, 0.10, 0.15 and 0.20) ceramic

| System | Composition | Crystal Structure | Lattice Parameter (Å) | Unit Cell Volume $(Å)^3$ | Crystallite Size (nm) |
|---|---|---|---|---|---|
| $Y_{2/3}Cu_3Ti_{4-x}Fe_xO_{12}$ | $x$ = 0.00 | Cubic | 7.4983 | 421.5833 | 68 ± 6 |
| | $x$ = 0.05 | Cubic | 7.5149 | 424.3867 | 64 ± 9 |
| | $x$ = 0.10 | Cubic | 7.5339 | 427.6257 | 62 ± 8 |
| | $x$ = 0.15 | Cubic | 7.5173 | 424.7931 | 60 ± 7 |
| | $x$ = 0.20 | Cubic | 7.5200 | 425.2557 | 58 ± 6 |

## 6.2.3 Scanning Electron Microscopic and Energy Dispersive X-ray Spectroscopic Studies

The scanning electron micrographs (SEM) of the fractured surfaces of all the five compositions of $Y_{2/3}Cu_3Ti_{4-x}Fe_xO_{12}$ ceramics sintered at 1000 $^{\circ}$C for 12h are shown in Fig 6.4(a-e). The SEM micrograph exhibits non-uniform grain size distribution consisting of bimodal nature with frequent segregation. The microstructure is dominated by small smooth grains with some pores. The grains have geometrical patterns like spherical, cylindrical and cubical in Fig 6.4(a-d) while some are hexagonal in Fig 6.4(e). It is clear from the variation in sizes of the grain that they are still in growing condition. The bimodal grain size distribution contains regions of fine grains about ~0.5-1 μm and regions of extremely large grains about ~1.5-3.5 μm for all compositions with a high degree of segregation. The composition of smaller and larger grains coincides with the stoichiometry of the chemical formula of $Y_{2/3}Cu_3Ti_{4-x}Fe_xO_{12}$ (where $x$ = 0.00, 0.50, 0.10, 0.15 and 0.20) is also supported by EDX results. The variation in grain size thereby leading to abnormal grain growth may be due to the presence of CuO rich phase at the grain boundary of the ceramic.

Fang *et al.* (2007) *also* reported the presence of CuO along the grain boundary which transforms into the liquid phase during sintering and may induce discontinuous grain growth. It is in agreement with the SEM micrograph of Fig 6.4. The CuO phase may contribute significant effects to promote the grain growth and densification of YCTFO samples. Fig 6.4(a) shows a discontinuous grain growth for the undoped YCTO ceramic ($x$ = 0.00). However, a continuous grain growth can be seen clearly for all the samples with doping of iron with a decrease in the average grain size from 0.61-5.2 μm for smaller grains and 3.14-2.30 μm for larger grains. The doping of iron has effectively prevented the growth of large grains and average grain sizes are approximately 0.5~3.5 μm which is independent of $Fe^{3+}$ concentration (Fig. 6.4 b-d). It indicates that the doping of iron with variable concentration can reduce the grain size of YCTFO ceramic and improve the density. It is also established that the increase in sintering temperature significantly promote the grain growth and microstructural densification. With the decrease in average size to those of smaller and larger grain, porosity decreases leading to more compactness of YCTFO ceramics. It has been reported in the literature that below 1μm, the dielectric constant decreases significantly with grain size. As the grain size approaches to 0.5- 1.5 μm, various types of stress operating in the grain suppress the domain and the dielectric constant falls to approximately 1000 (Moulson *et al.*, 2003). Such kind of relation between the grain size and dielectric constant value is very well observed for different YCTFO ceramic samples. Besides grain size in the range of 0.5-1.5 μm, all iron doped YCTO ceramic exhibits a low dielectric constant value (ε ~ 380, 351, 881, 1275) than the pure YCTO ceramic (ε ~ 2198) with grain size in the range of 1-3μm. It may be due to porosity, compactness of grain and the structural quality of the material. It is also evident from the Fig. 6.4 that YCTFO ceramic samples exhibit some degree of porosity. The calculated values of porosity are listed in the Table 6.2. The observed porosity may be attributed to the formation of oxygen vacancies during sintering. It may be also due to lower sintering temperature. An increase in sintering temperature may lead to decrease in porosity owing to the grain growth phenomena. Moreover, the porosity also depends upon processing route, samples prepared by Pechini method and co-precipitation method exhibit a lower extent of porosity than those prepared by other processes at the same sintering temperature (Niwa *et al.*,

2012). It was also observed that doping of Fe in YCTO ceramic resulted in decrease in density and increase in porosity. As density and porosity affect the microstructure as well as dielectric properties of the ceramic, their values for different $Y_{2/3}Cu_{3-x}Ti_{4-x}Fe_xO_{12}$ ceramics were also determined and are listed in Table 6.2. The bulk densities of the samples were found to be 1.19. 1.67, 1.33, 1.29, and 1.28 for $x$ = 0.00, 0.05, 0.10, 0.15 and 0.20, respectively, considering the theoretical density of 5.995 g/cc for YCTO (Liang *et al*., 2012). Such variation in densities of these samples may be due to the presence of some pores in YCTFO samples.

**Table 6.2**: Pellet Dimension, density and Porosity characteristic for different $Y_{2/3}Cu_3Ti_{4-x}Fe_xO_{12}$ ceramic sintered at 1000 $^{\circ}$C for 12 h.

| System | Composition | Pellet Dimension (mm) | | Density | | Porosity | |
|---|---|---|---|---|---|---|---|
| | | Thickness | Diameter | Theoretical | Bulk | Bulk | Apparent |
| $Y_{2/3}Cu_{3-x}Ti_{4-x}Fe_xO_{12}$ | $x$ = 0.00 | 3.5 | 12.5 | 5.995 | 1.195 | 80.06 | 22.02 |
| | $x$ = 0.05 | 2.0 | 9.0 | 5.950 | 1.167 | 80.38 | 11.19 |
| | $x$ = 0.10 | 3.0 | 9.0 | 5.895 | 1.337 | 77.32 | 30.38 |
| | $x$ = 0.15 | 2.0 | 9.0 | 5.925 | 1.291 | 78.21 | 18.67 |
| | $x$ = 0.20 | 2.0 | 10.5 | 5.909 | 1.287 | 78.21 | 14.16 |

Fig. 6.5 shows EDX spectra of a grain of different compositions of $Y_{2/3}Cu_3Ti_{4-x}Fe_xO_{12}$ which confirms the presence of Y, Cu, Ti, Fe and O elements. Quantitative data for the atomic and the weight percentage of the elements present in the grain of YCTFO obtained from EDX data are shown in Table 6.3. The atomic percentage of Y, Cu, Ti, Fe and O in different compositions of $Y_{2/3}Cu_3Ti_{4-x}Fe_xO_{12}$ ceramics was as per expected stoichiometry.

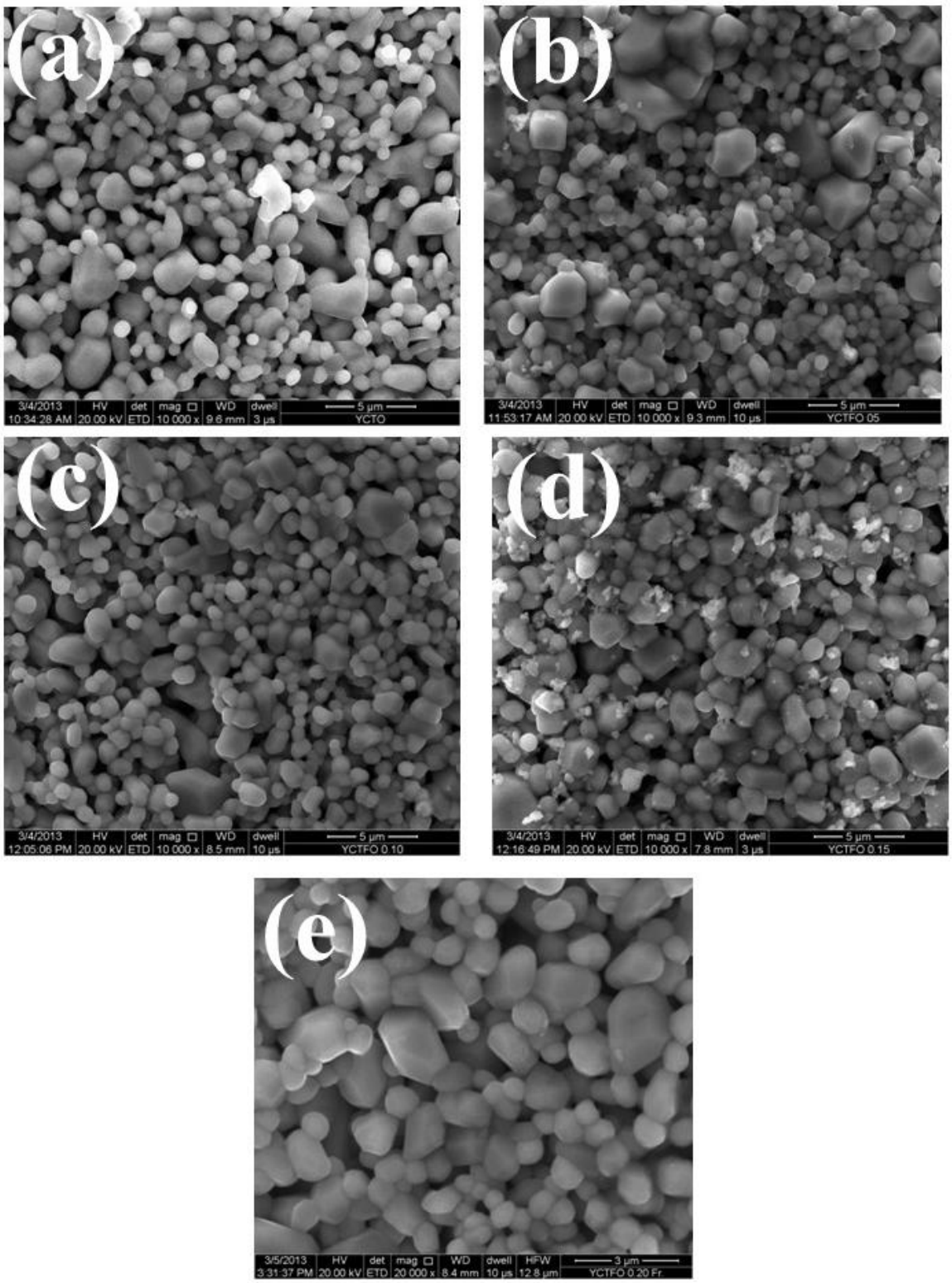


Figure 6.4: SEM micrographs of $Y_{2/3}Cu_3Ti_{4-x}Fe_xO_{12}$ (a) $x$ = 0.00, (b) $x$ = 0.05, (c) $x$ = 0.10, (d) $x$ = 0.15 and (e) $x$ = 0.20 sintered at 1000 $^{\circ}$C for 12h.

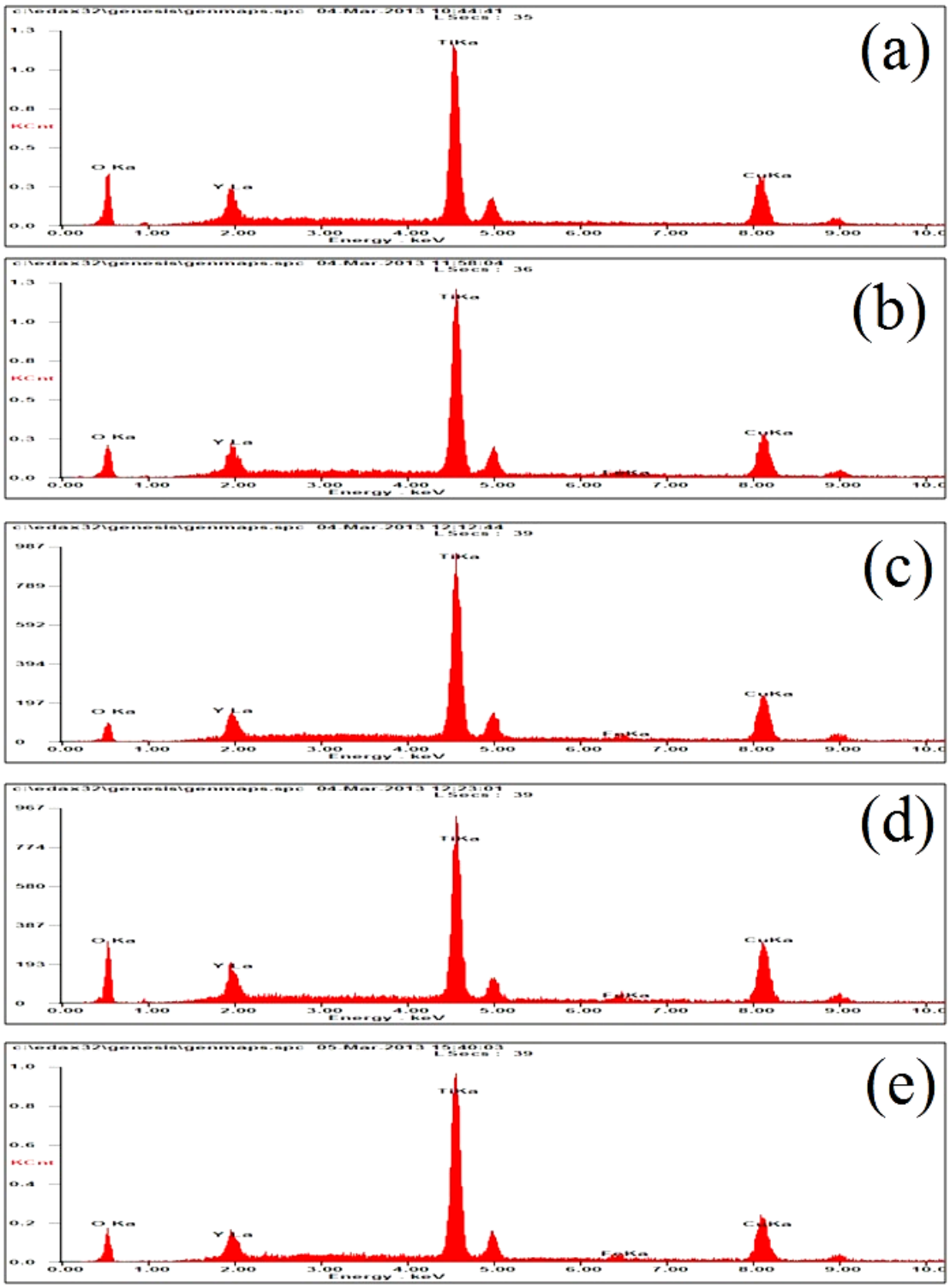


Figure 6.5: EDX spectra of $Y_{2/3}Cu_3Ti_{4-x}Fe_xO_{12}$ (a) $x$ = 0.00, (b) $x$ = 0.05, (c) $x$ = 0.10, (d) $x$ = 0.15 and (e) $x$ = 0.20 sintered at 1000 $^{\circ}$C for 12h.

**Table 6.3**: Atomic percentage and weight percentage of elements for $Y_{2/3}Cu_3Ti_{4-x}Fe_xO_{12}$ ceramic ($x$ = 0.00, 0.05, 0.10, 0.15, 0.20) sintered at 1000 °C for 12 h.

| System | Composition | Region | Wt% | | | | At% | | | | | |
|---|---|---|---|---|---|---|---|---|---|---|---|---|
| | | | **Y** | Cu | Ti | Fe | O | **Y** | Cu | Ti | Fe | O |
| $Y_{2/3}Cu_{3-x}Ti_{4-x}Fe_xO_{12}$ | x =0.00 | (Grain) | 08.94 | 33.76 | 33.36 | ---- | 23.95 | 03.56 | 18.80 | 24.65 | ---- | 52.99 |
| | x = 0.05 | (Grain) | 08.40 | 32.94 | 37.91 | 1.68 | 19.06 | 03.60 | 19.74 | 30.14 | 01.14 | 45.37 |
| | x = 0.10 | (Grain) | 08.07 | 36.76 | 40.21 | 1.65 | 13.31 | 03.38 | 24.41 | 35.42 | 01.25 | 35.09 |
| | x = 0.15 | (Grain) | 08.28 | 36.67 | 29.95 | 1.99 | 36.67 | 03.36 | 20.80 | 22.53 | 01.28 | 20.80 |
| | x = 0.20 | (Grain) | 07.91 | 33.19 | 38.28 | 2.19 | 18.43 | 03.42 | 20.08 | 30.72 | 01.51 | 44.28 |

.

## 6.2.4 Atomic Force Microscopic Study

The surface topography of $Y_{2/3}Cu_3Ti_{4-x}Fe_xO_{12}$ ceramic, with composition $x$ = 0.10, was studied with the help of Atomic Force Microscopy. These images were obtained by a thin film deposition on amorphous glass substrate in a tapping mode. Fig. 6.6(a) depicts the two-dimensional AFM micrograph of $Y_{2/3}Cu_3Ti_{4-x}Fe_xO_{12}$ ($x$ = 0.10) thin film which is smooth and compact. The average grain size and average diameter of grain estimated to be 22.9 nm (Fig. 6.7a) and 33.7 nm (Fig. 6.7b) while the grains were homogeneously mounted over the substrate of an area 0.00107 $\mu m^2$ (Fig. 6.7c). The 2-Dimensional and 3-Dimensional surface roughness of a sample is investigated by amplitude and height analysis parameters, respectively. The amplitude analysis parameters mainly includes average roughness, root mean square roughness, maximum peak to valley height roughness, ten-point mean height roughness, skewness roughness and kurtosis roughness. Through the roughness parameters, the surface condition of the entire measured length or area will be evaluated in terms of peak and valley (Raposos *et al* 2007).

Based upon the statistical study of total 252 grain ensembles within the length 3.52 μm and scanning area 5 μm × 5 μm for two-dimensional AFM image of surface of YCTO thin film, the value of average roughness ($R_a$) and Root mean square

roughness ($R_q$) was estimated to be 1.266 and 1.424 nm. The average roughness gives the deviation of the calculated mean height over the measured area while Root mean square roughness demonstrates the standard deviation of the surface height over the measured area. The Maximum peak to valley height roughness ($R_t$) which summarizes the total roughness of the measured area was found to be 4.064 nm whereas the Ten-points mean height roughness ($R_z$) shows the mean height difference between the average of the five highest peaks and the five lowest valleys in the evaluation surface was found to be 3.956 nm.

The functional parameters such as skewness ($R_{Sk}$) and kurtosis ($R_{Ku}$) moments are used to measure the asymmetry and the flatness of the thin film, respectively. The Skewness roughness ($R_{sk}$) is used to measure the profile symmetry of the mean line was found to be 0.415, while kurtosis roughness ($R_{ku}$) is used to measure the surface sharpness which is in fact, the distribution of the spikes above and below the mean line was found to be 1.668 which is less than 3. Apart from average roughness, the lower positive values of skewness roughness ($R_{sk}$) imply for the smoothness of surface with predominant peaks while higher positive value for kurtosis roughness ($R_{ku}$) indicating that the surface of scanned area of YCTFO thin film is slightly bumpy in nature due to the appearance of low number of high peaks and low valleys on the surface. It is more evident from the 3D image (Fig. 6.6 C). As kurtosis value is less than three, such distribution curve is called Platykurotic which is usually characterized by relatively few high mountain and valley.

Fig. 6.6(b) shows the grains and grain boundary regions in YCTFO thin film. It exhibits compact structure with granular morphology, buffer layer, plates like grains and clear grain boundary. Fig. 6.6(c) exhibits its three-dimensional surface morphology exhibits several peaks corresponding to grain with compact structure. Based upon the statistical study of total $1.2 \times 10^5$ grains within the scanning area 5 μm × 5 μm and sampling and evaluation area 25.019 $\mu m^2$ for the three-dimensional AFM image of YCTFO thin film surface, the value of average roughness (Sa), Root mean square roughness (Sq), maximum peak to valley height roughness ($S_z$) and 10-points mean height roughness ($S_{10z}$) was estimated to be 0.295, 0.406, 6.534 and 5.964 nm, while skewness ($S_{ku}$) and kurtosis ($S_{sk}$) was found to be -0.411 and 6.895. A negative value of skewness is the indication of planar surface with some valleys

below the average line. The Kurtosis value greater than 3, confirming the distribution curve to be Leptokurtoic which in turn, is characterized by many high peak but low valley. It is also agreement with the 3D AFM-image. 3D surface analysis refines the data and findings obtained in 2D mode in a more accurate way.

The surface roughness parameters of the tested sample in 2D and 3D AFM study of YCTFO thin film, deduced with the help of NOVA software are summarized in Table 6.4.

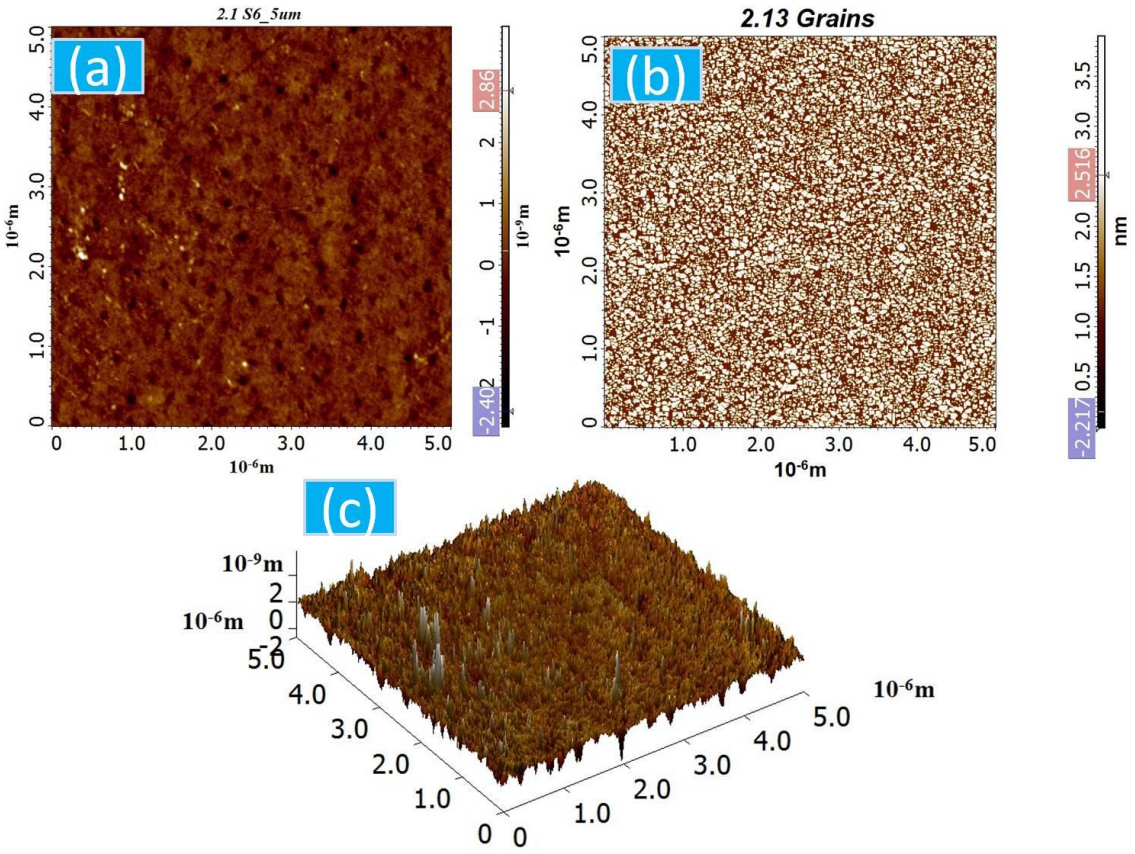


Figure 6.6: 2- dimensional AFM micrograph of thin film of (b) 2-dimensional AFM micrograph showing grain boundary (c) 3-dimensional AFM micrograph of sintered $Y_{2/3}Cu_3Ti_{4-x}Fe_xO_{12}$ ($x$ = 0.10) ceramic.

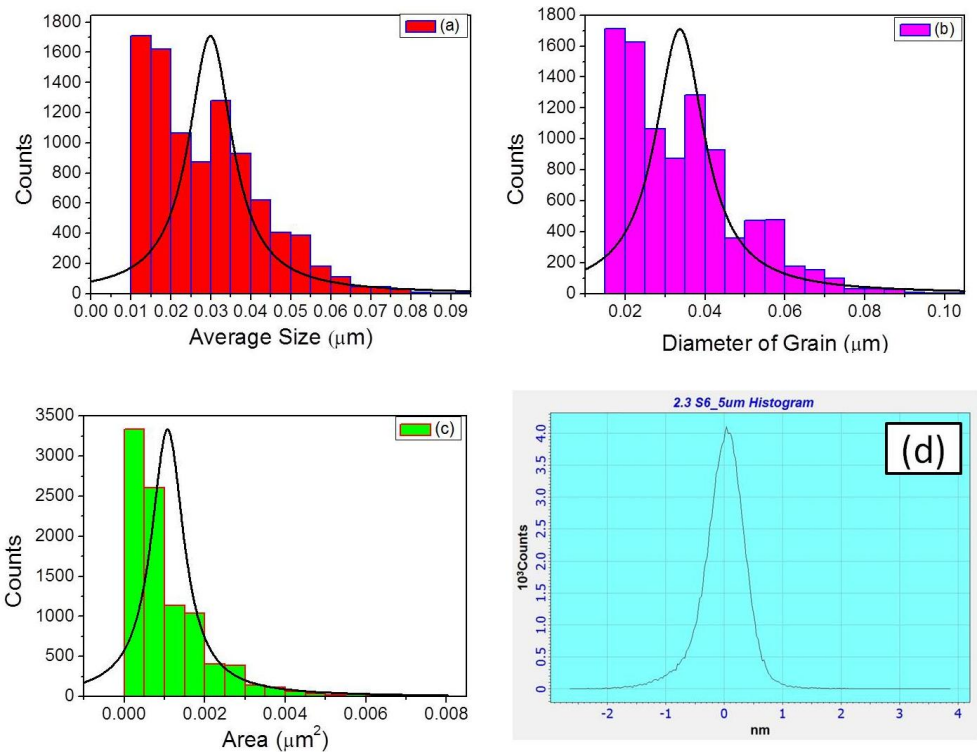


Figure 6.7: Different histograms for sintered $Y_{2/3}Cu_3Ti_{4-x}Fe_xO_{12}$ ($x$ = 0.10) ceramic exhibiting (a) Average size (b) Diameter of grains (c) Area of grains and (d) Average 3 -dimensional surface roughness.

**Table 6.4:** The surface roughness parameters of $Y_{2/3}Cu_3Ti_{4-x}Fe_xO_{12}$ ($x$ = 0.10) thin film obtained by 2D- and 3D- AFM-image mapping.

| **Roughness Details** | **Parameters** | |
|---|---|---|
| | **Amplitude (2D)** | **Height (3D)** |
| Average /Arithmetic | 1.854 | 1.517 |
| Root Mean Square | 2.288 | 1.978 |
| Maximum peak to valley height roughness | 10.559 | 26.979 |
| Ten-points mean height roughness | 8.328 | 21.085 |
| Skewness | 0.0136 | 0.473 |
| Kurtosis | 2.641 | 5.789 |

## 6.2.5 Transmission Electron Microscopy

The bright field TEM image of YCTFO ceramic sintered at 1000 °C for 12h is represented in Fig 6.8(a-c). The distinguished TEM image with the concentration of $x$ = 0.00, 0.05 and 0.10 only is produced here. The particles of different compositions of $Y_{2/3}Cu_3Ti_{4-x}Fe_xO_{12}$ (where $x$ = 0.00, 0.05 and 0.10) are well dispersed with high extent of agglomeration. The average particles size of the ceramic was found to be in the range of 60 ± 20, 35 ± 5 and 20 ± 7 nm for composition $x$ = 0.00, 0.05 and 0.10, respectively.

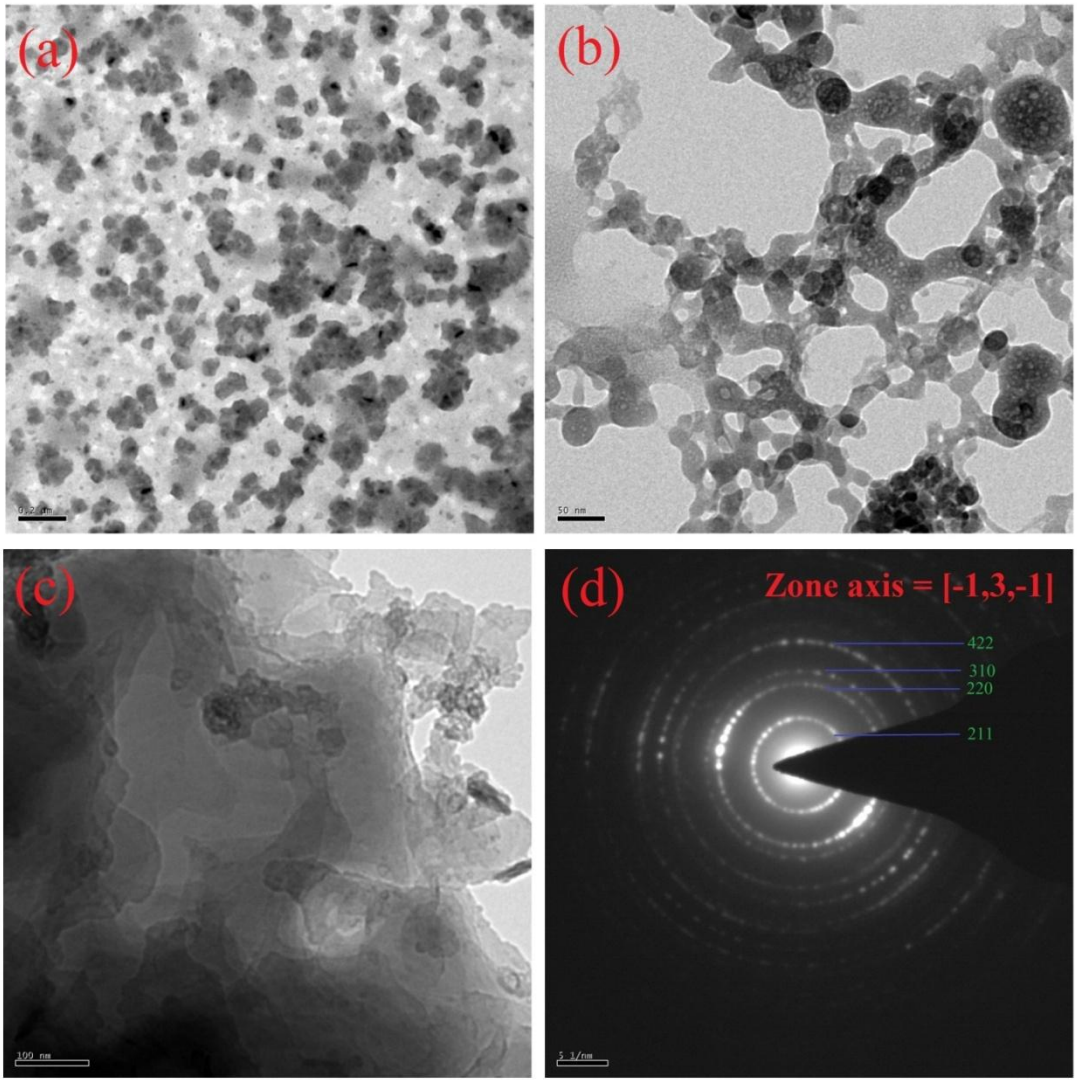


Figure 6.8: Bright field TEM micrographs of sintered $Y_{2/3}Cu_3Ti_{4-x}Fe_xO_{12}$ ceramic (a) $x$ = 0.00 (b) $x$ = 0.05 (c) $x$ = 0.10 (d) SEAD pattern for $x$ = 0.10.

The lattice parameter calculated from the electron diffraction pattern is also in agreement with that obtained from the XRD data. However, the particle size obtained by TEM analysis is smaller than that from XRD results for the compositions $x$ = 0.05 and 0.10, because a crystallite may consist of several particles. It is important to note that with the help of TEM particle size is measured but with XRD we measure the crystallite size which is the coherent diffracting crystalline domains (crystallite), which is different from the particle size. One particle can be constituted by several crystalline domains (crystallites), this is why always particle size has to be bigger than crystallite (domain) size, or in case of small nano particles both of them can be the same. But the domain size (calculated from XRD) can't be bigger than particle size obtained from TEM (Carter *et al*., 2009).

TEM diffraction patterns were indexed on the basis of body centered cubic perovskite structure. The corresponding selected area electron diffraction (SAED) pattern of TEM image for YCTFO ceramic is shown in Fig. 6.8(d). As the corresponding selected area electron diffraction (SAED) pattern of TEM image for different samples are more or less the same, SAED picture for composition $x$ = 0.10 only is produced here. The presence of a few clear rings in SAED pattern again confirms the formation of the polycrystalline phase of thermodynamically stable YCTFO ceramic.

## 6.2.6 P-E Loop measurement

The origin of polarization and ferroelectric behavior of ceramic may be justified with the help of polarization electric (P-E) Loop tracer technique. PE hysteresis loop is related to its energy storage ability and it displays significant material property of dielectric materials. This loop can be discussed in terms of three important parameters viz. remnant polarization ($P_r$), saturated polarization ($P_s$) and coercive field ($E_c$) under the external electric field. The PE hysteresis loop obtained at 308 K for $Y_{2/3}Cu_3Ti_{4-x}Fe_xO_{12}$ ($x$ = 0.10) ceramic is shown in Fig. 6.9. The value of remnant polarization (Pr), saturation polarization and coercivity ($E_C$) are found to be 0.0.505μC/cm$^2$, 1.934μC/cm$^2$ and 1.232 kV/cm, respectively when the applied voltage is 2.699 kV/cm without an electric breakdown. This may be due to the alignment of domains present in the ceramic which increases with temperature in absence of

electric field. Another reason may be the display of high dielectric constant phenomenon, contributing significantly to the relaxor-ferroelectric behavior (Raya *et al.*, 2013).

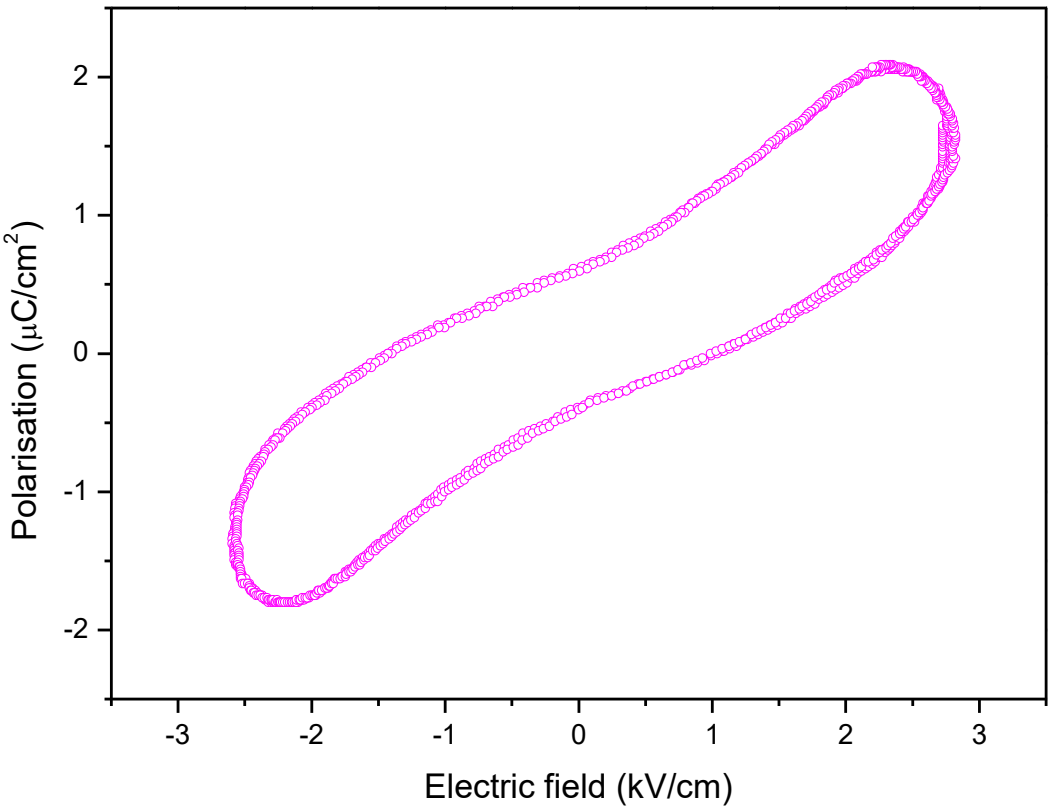


Figure 6.9: P-E hysteresis loop of $Y_{2/3}Cu_3Ti_{4-x}Fe_xO_{12}$ ($x$ = 0.10) ceramic at 308 K.

## 6.2.7 Dielectric Behavior

Fig. 6.10 exhibits the temperature dependence of dielectric constant (ε) and dielectric loss (tan $\delta$) measured at 100 Hz for $Y_{2/3}Cu_3Ti_{4-x}Fe_xO_{12}$ (YCTFO) ceramics. It is clearly observed from Fig 6.10(a) that the YCTFO ceramic with the concentration of iron, $x$ = 0.20 exhibits a step-like increase in dielectric constant with increasing temperature. Along with this, dielectric peaks are also observable for almost all iron doped YCTFO compositions with $x$ = 0.00, 0.10, 0.20 near temperature 350-360 K. But the dielectric peak appears to be suppressed one for compositions $x$ = 0.05 and 0.15, and it exhibit almost temperature independent behavior beyond temperature 425 K. The appearance of peaks in dielectric constant with temperature suggests the presence Debye-like relaxation in YCTFO ceramics. In general, one Debye-like

relaxation is accompanied by the appearance of dielectric loss peak or hump in tan $\delta$–T plot. As shown in Fig 6.10(b), only one dielectric loss peak is observed around 360 K for YCTFO ceramics. However, the peak gets suppressed in the case of $x$ = 0.15. The presence of dispersion peaks as shown in Fig 6.10(a) & (b) in the low-temperature region (300-400 K) gets intensified in both ε-T and tan $\delta$–T plots. It may be attributed to increasing the grain boundary resistance. Thus, the low-temperature dielectric relaxation in YCTFO ceramics supports the grain boundary effects. The value of dielectric constant as well tan $\delta$ increases at high-temperature (Fig 6.10) for $x$ = 0.20 composition may be attributed to the high electrical conductivity of the sample.

Fig. 6.11 illustrates the variation of real (ε′) and imaginary part of dielectric constant (ε″) with frequency (2Hz -5MHz) for YCTFO ceramic sintered at 1000 $^{\circ}$C for 12 h. The values of ε′ of YCTFO ceramic with composition $x$ = 0.00, 0.05, 0.10, 0.15 and 0.20 are 100837, 32948, 43065, 29958 and 32376, respectively (Fig 6.11a). All YCTFO samples exhibit a continuous decrease in dielectric constant with frequency. The decrease in ε′ is rapid in the low frequency range (2 Hz-100 Hz) but slow in the higher frequency range (1 kHz to 5 MHz). A rapid decrease in dielectric constant with frequency may be due to the contribution of space charge accumulation at the interface which leads to polarization of the ionic medium and hence the value of ε′ increases. In fact, in the high-frequency regions, the periodic reversal of the field takes place so rapidly that there is no charge accumulation at the interface, resulting into a constant ε′ value (Tareev 1975). A large value of dielectric constant under frequency 2-100 Hz may be also be attributed to the electrode contact and a rapid decrease in ε′ value at a frequency, $f$ > 100 Hz may be due to conductive grains.

The frequency dependence of the imaginary part of dielectric constant (ε″) at room temperature for all compositions is shown in Fig 6.11(b). All the curves show an appreciable decrease in the magnitude of ε″. At high frequencies, the decrease in ε″ is much lower than the one occurring at low frequencies. The dependence of ε″ with frequency is associated with losses due to the conduction mechanism.

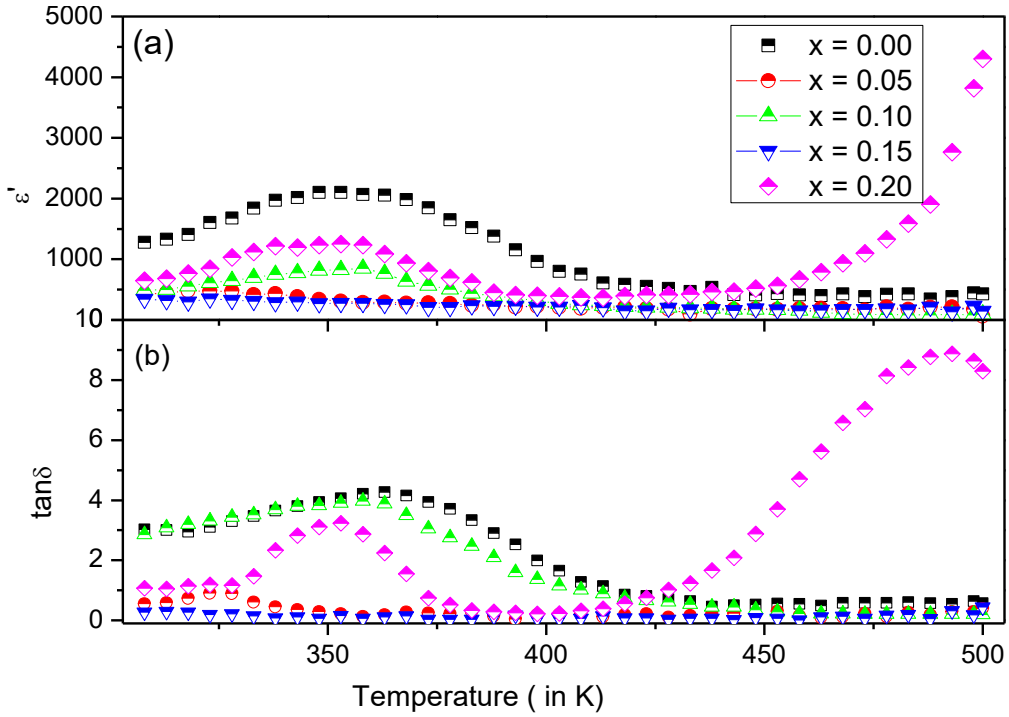


Figure 6.10: Variation of dielectric constant (ε′) and loss tangent (tan $\delta$) with temperature at 100 Hz frequency for sintered $Y_{2/3}Cu_3Ti_{4-x}Fe_xO_{12}$ ceramic ($x$ = 0.00, 0.05, 0.10, 0.15 and 0.20).

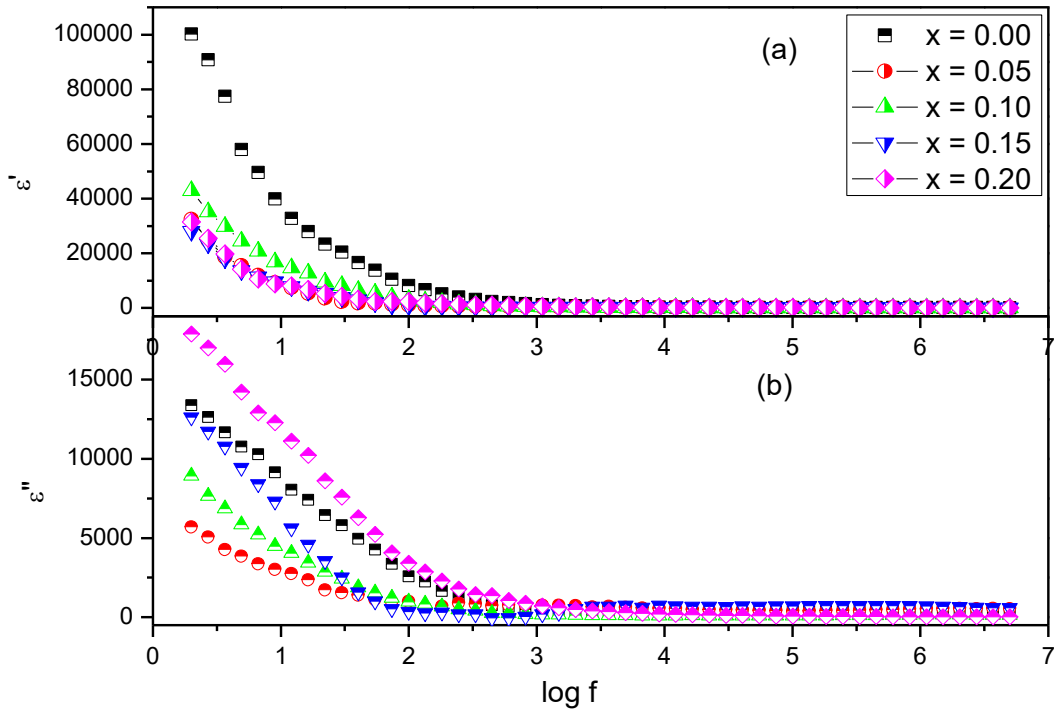


Figure 6.11: Variation of (a) real dielectric constant (ε′) and (b) imaginary dielectric constant (ε″) with frequency at 308 K for $Y_{2/3}Cu_3Ti_{4-x}Fe_xO_{12}$ ($x$ = 0.00, 0.05, 0.10, 0.15 and 0.20) ceramic.

Fig. 6.12 shows the variation of dielectric loss (tan $\delta$) with frequency at room temperature (308 K) for $Y_{2/3}Cu_3Ti_{4-x}Fe_xO_{12}$ ceramics. The value of tan $\delta$ decreases rapidly over the entire frequency range. the dielectric loss for all compositions show a sharp decreasing trend up to 100 Hz and then a small rising at 1 kHz for $x$ = 0.00, 0.10, 0.20 but after 1 kHz the dielectric losses decreases sharply, however, the dielectric losses for YCTFO ceramic are higher at a low frequency below 10 kHz. Further the tan $\delta$ value decreases significantly at a higher frequency form 10 kHz-5MHz which may be which may be attributed to the presence of small interfacial polarization in the YCTFO ceramic.

It is also clear from Fig. 6.12 that the curve passes through a higher to a minimum tan $\delta$ at 1 kHz frequency. The dielectric loss decreases with increase in iron content in different YCTFO samples. The sample with $x$ = 0.15 and 0.20 possess comparatively lower dielectric loss while sample with $x$ = 0.00 exhibits much higher dielectric loss. For almost all compositions of YCTFO ceramics $x$ = 0.00-0.20, the tan $\delta$ value decreases showing a clear hump at or below 10 kHz.

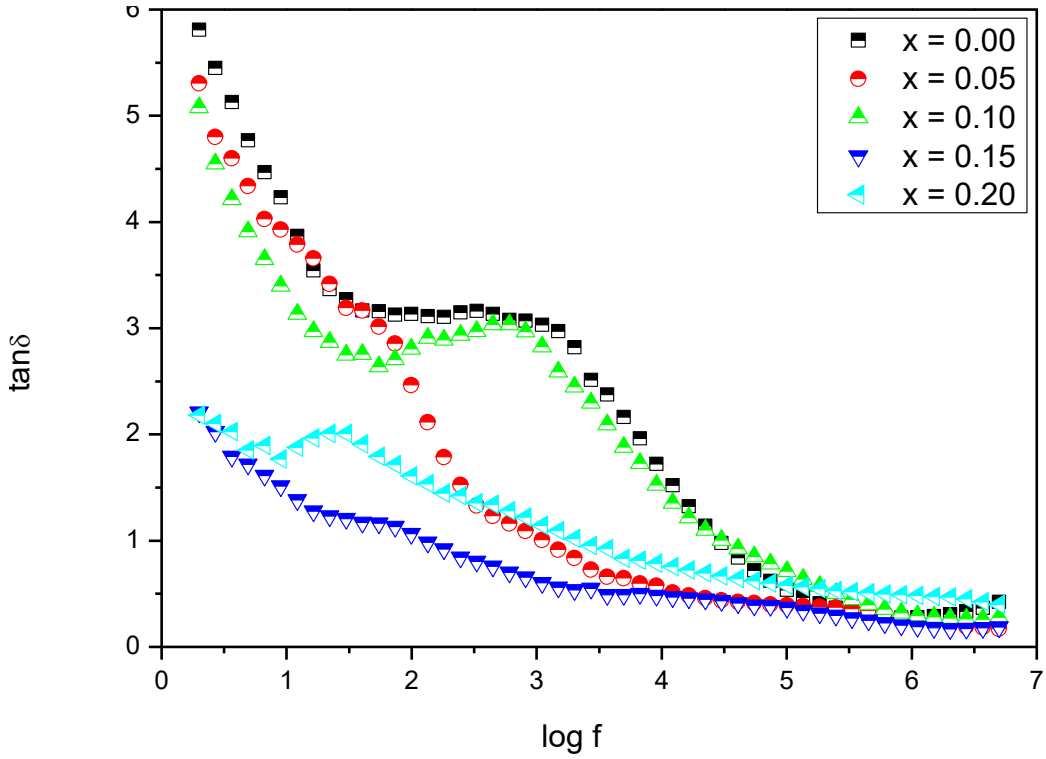


Figure 6.12: Variation of tan δ with frequency at 308 K for $Y_{2/3}Cu_3Ti_{4-x}Fe_xO_{12}$ ($x$ = 0.00, 0.05, 0.10, 0.15 and 0.20) ceramic.

But the curve for $x$ = 0.15, 0.20 got relatively flat, without any characteristic hump. These were similar to some extent to those of variation in dielectric constant value with increasing frequency. Higher concentration of iron doping may introduce more oxygen vacancies and space charges producing thereby dielectric relaxation peaks which cause more dielectric loss. The anomalous behavior of variation in dielectric loss of Fe at $x$ = 0.00, 0.10, 0.20 to those of $x$ = 0.05, 0.15 may be due to microstructural differences, especially in grain sizes, its distribution and grain growth phenomena of both small and larger sized grain different in YCTFO ceramic. Such anomalous trend was also reflected in the variation of ε-T and tan $\delta$-T in Fig. 6.10 and in Fig. 6.12, respectively, supporting thereby the fact that a proportionate introduction of iron flattens the dielectric constant appreciably with a significant reduction in dielectric loss (tan $\delta$) simultaneously in the YCTFO ceramic.

The mechanism of dielectric relaxation in $Y_{2/3}Cu_3Ti_{4-x}Fe_xO_{12}$ ceramic could be interpreted reasonably by the modified mixed valent structure in transition metallic oxide ceramic. In a mixed valent structure, the dielectric relaxation is supposed to be due to loss of traces of oxygen, creating thereby oxygen vacancies during sintering at high temperature. This is in accordance with Kroger-Vink notation of defects reaction;

$$O_o \leftrightarrow \frac{1}{2}O_2 + V_o^{\bullet\bullet} + 2e^- \tag{6.2}$$

where all the species are written in accordance with Kroger-Vink notation of defects (Norby et al., 2010). Electrons released in this reaction may be captured by $Cu^{2+}$ or $Ti^{4+}$ to produce $Cu^{+}$ or $Ti^{3+}$ respectively as below:

$$2Cu^{2+} + 2e^- \rightarrow 2Cu^{+} \tag{6.3}$$

$$2Ti^{4+} + 2e^- \rightarrow 2Ti^{3+} \tag{6.4}$$

The probability of formation of $Ti^{3+}$ ($3d^1$) is negligible in comparison to $Ti^{4+}$ ($3d^0$) as per stability criteria. On the other hand, $Cu^{+}$ with $3d^{10}$ configuration is a stable state of Cu due to the inert gas configuration. $Cu^{+}$ ions on $Cu^{2+}$ site will carry an effective negative charge, viz $Cu^{+}_{Cu^{2+}}$. These negative charges may form dipoles

with $V_o^{\bullet\bullet}$ as $2Cu^{+}_{Cu^{2+}} \rightarrow V_o^{\bullet\bullet}$. These diploes can change their orientation either by hopping of electron among $Cu^{+}$ and $Cu^{2+}$ or due to jumping of oxygen ions through vacant oxygen sites around the $CuO_4$ square or $TiO_6$ octahedral giving rise to orientation polarization (Sun et al., 2008). It leads to increase in the conductivity and so the dielectric loss as observed in Fig 6.12, discussed later. An increase in conductivity makes the grain of such mixed-valent ceramics semiconducting. The rapid decrease in dielectric constant of $Y_{2/3}Cu_3Ti_{4-x}Fe_xO_{12}$ with different $Fe^{3+}$ concentration at a higher frequency may be due to the inability of dipoles to keep stepping with the change in frequency. It is the reason for high-frequency dielectric relaxation of YCTFO ceramic which gets induced by a mixed valent structure of $Cu^{+}/Cu^{2+}$ and $Ti^{3+}/Ti^{4+}$ while the low-frequency dielectric relaxation of YCTFO ceramic may be regarded as a result of oxygen vacancies created during the sintering process. The duo factor, the mixed valent structure and oxygen vacancies may significantly contribute for the origin of the high dielectric constant of YCTFO ceramic. Along with these two factors interfacial polarization and formation of the barrier layer at grain and grain boundaries interface significantly contribute to the high dielectric constant of YCTFO ceramic. Impedance analysis can further confirm the formation of barrier layers at the interface.

The decreasing value of both, ε and tan $\delta$ with increasing frequency are due to interfacial polarization. It arises due to micro-heterogeneities occurred in the ceramic with different extent of doping which, in turn, may be because of the slow diffusion-controlled thermochemical process used in their preparation, their calcination and sintering processes. Iron doping in $Y_{2/3}Cu_3Ti_4O_{12}$ (YCTO), lower downs the dielectric loss (tan $\delta$ ) but the same along with giving rise to higher values of dielectric constant as compared to the parent YCTO ceramic and it shows a stronger dependence on frequency as well as temperature. This limits the usefulness of these materials. It is expected that using different atmosphere during sintering and post-sintering; the above properties may be improved showing a positive direction for clues to decrease the dielectric loss to an appreciable extent for the potential application of YCTFO ceramic.

## 6.2.8 Impedance Analysis

Impedance analysis could support the dielectric behavior of different YCTFO samples in correlation with its microstructure. In order to understand the reasons for dielectric dispersion and formation of the barrier layer in YCTFO ceramic, the complex plane impedance (Z*) approach was adopted. Using this valuable analytical tool, we may gather information about the occurrence of multi-polarization processes simultaneously in the ceramic and their relaxation conditions. The effective contribution of grains, grain-boundaries and electrode specimen interface to the total resistance and capacitance, respectively can also be determined.

The concept of the simplest equivalent circuit consisting of a series of a network of three parallel RC elements can be applied to YCTFO ceramic. Normally, for all the three contributions, three circular arcs may be obtained at a lower temperature (below 273 K)consist of centers on or below the real axis Z′ depending on whether there is a single relaxation time for each of the above processes, or there is a distribution of relaxation times.

A representative Cole-Cole Plot for sintered YCTFO ceramics at a different concentration at room temperature is illustrated in Fig. 6.13. It clearly demonstrates the presence of two semi-circular arcs with different intercepts (except for $x$ = 0.20) which may be due to the grain boundary and electrode surface effects. On extrapolation, the intercept on Z′ axis is not found to be close to zero (Fig. 6.14). It suggests that there must be an existence of another semi-circle in higher frequency region beyond the measuring frequency range. The non-zero intercepts on Z′ axis yielding the grain resistance values extracted from Fig. 6.14 are shown in Table 6.5. The intercept at a high-frequency region is very tiny in comparison to the intercept at a low-frequency region. It indicates that the total resistance of YCTFO ceramics is mainly governed by the resistance of grain boundary ($R_{gb}$) i.e. $R_{gb} >> R_g$ where $R_{gb}$ and $R_g$ are the resistances of grain boundary and grain, respectively. It implies that the dielectric properties are mainly influenced by the physical characteristic of grain boundaries, for e.g. the real part of the permittivity, the resistivity of grain and grain boundaries and the thickness i.e. an exact ratio of the average grain size and the width of the grain boundary depletion layer. The exceptional behavior for the YCTFO

ceramic with concentration variant $x$ = 0.20 suggests the predominance of electrode effect at room temperature. Therefore, IBLC effect, a well-accepted explanation for dielectric phenomena in CCTO, can apply to reveal the dielectric response in different YCTFO ceramics. The observed dielectric characteristics of all the five concentration variant of YCTFO ceramics, as described under dielectric section may be attributed to the effect of special heterogeneous microstructure.

**Table 6.5:** Calculated values of resistances of grain and grain boundary at room temperature (308 K) for $Y_{2/3}Cu_3Ti_{4-x}Fe_xO_{12}$ (where $x$ = 0.00, 0.50, 0.10, 0.15 and 0.20) nano-ceramic sintered at 1000 $^{\circ}$C for 12 h.

| **Composition** | **$R_g$(Ω)** | **$R_{gb}$(Ω)** | **$C_g$ (pF)** | **$C_{gb}$ (nF)** |
|---|---|---|---|---|
| $x$ = 0.00 | 410 | $1.28\times 10^5$ | - | 9.13 |
| $x$ = 0.05 | 379 | $1.21\times 10^5$ | - | 9.22 |
| $x$ = 0.10 | 368 | $1.94\times 10^5$ | - | 9.25 |
| $x$ = 0.15 | 345 | $1.34\times 10^5$ | - | 9.29 |
| *$x$ = 0.20* | 296 | $1.08\times 10^5$ | - | 9.33 |

Fig 6.15 illustrates the variation of the imaginary part of impedance Z″ with frequency at room temperature for YCTFO ceramics. It displays the appearance of two relaxation peaks in two distinct ranges of frequencies except for $x$ = 0.20. The relaxation peaks at lower frequency region may be due to the electrode effects whereas in higher frequency region may be attributable to grain boundary effects. The intensity of peaks get suppressed and slightly shifted to the high-frequency region on increasing temperature which confirms the existence of a temperature-dependent Maxwell-Wagner dielectric relaxation. The electrode resistance appears at all measured temperature which may be due to electrode polarization effects present in the YCTFO ceramic. Interestingly, the inflection point in the impedance plots is the same as that of relaxation peaks in the corresponding ε″ vs. log f (Fig. 6.11 b) plot. It gives a clear evidence for the occurrence of Maxwell-Wagner relaxation. A decrease in the intensity peak of different iron concentration in YCTFO ceramics also suggests

a thermally activated dielectric response. In other words, we can say the dielectric property of YCTFO ceramic is due to the combined effect of grain and grain boundaries mainly.

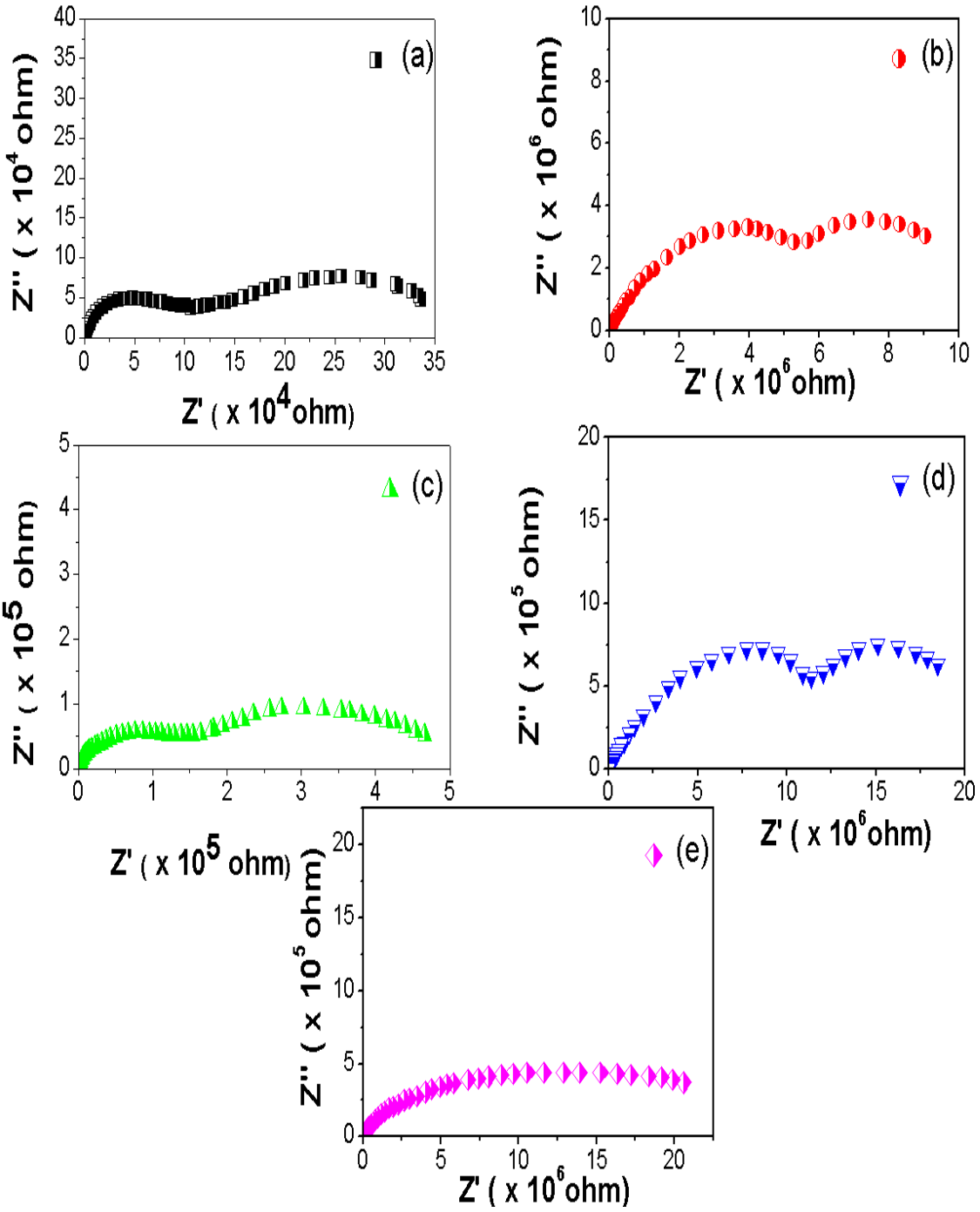


Figure 6.13: Complex impedance plane plots (Z′ vs Z″) at room temperature (308 K) for sintered $Y_{2/3}Cu_3Ti_{4-x}Fe_xO_{12}$ ceramic (a) $x$ = 0.00, (b) $x$ = 0.05, (c) $x$ = 0.10, (d) $x$ = 0.15 and (e) $x$ = 0.20.

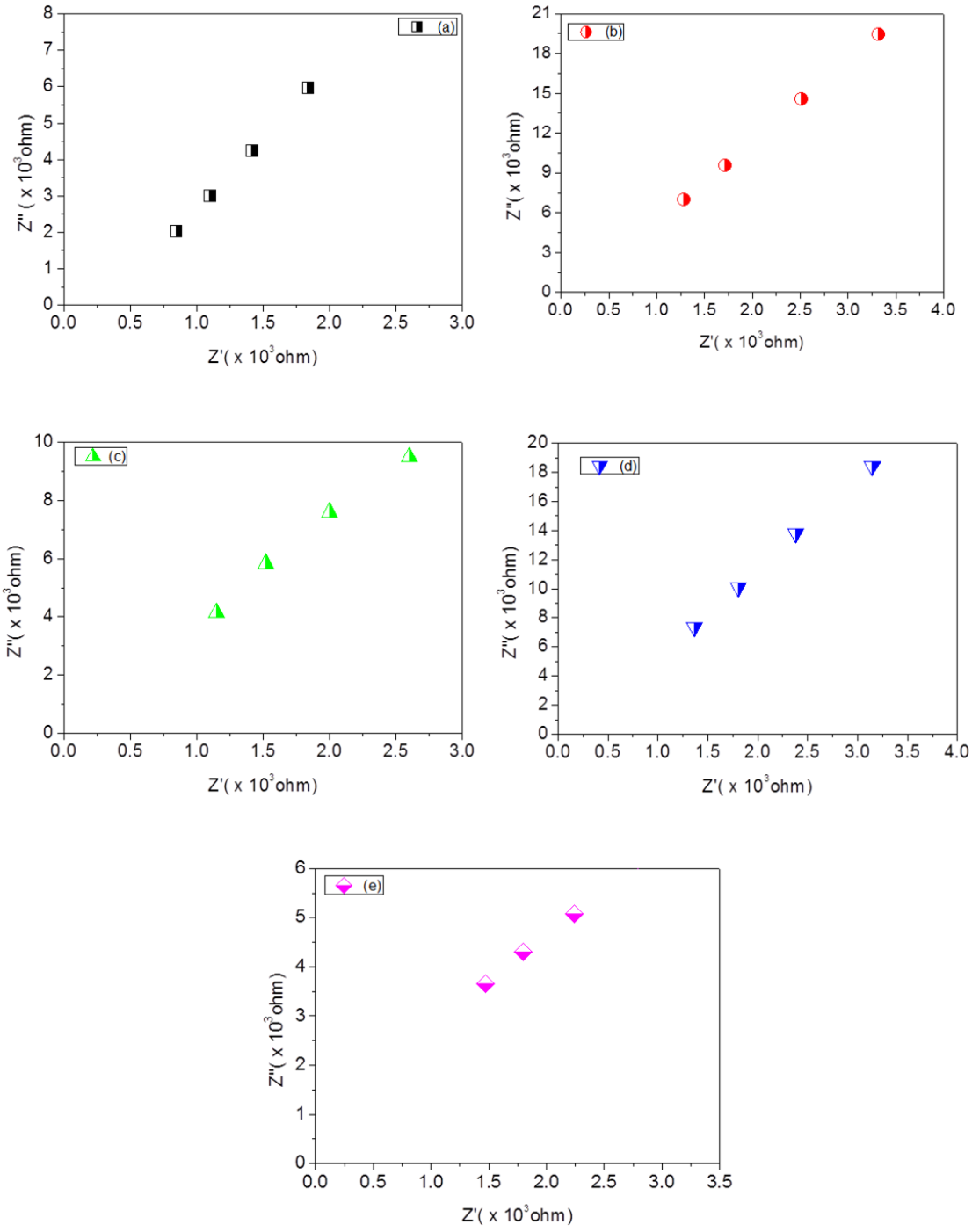


Figure 6.14: Extrapolation of Z′ vs Z″ plot in the higher frequency range at room temperature (308 K) to get resistance of grain for $Y_{2/3}Cu_3Ti_{4-x}Fe_xO_{12}$ ceramic (a) $x$ = 0.00, (b) $x$ = 0.05, (c) $x$ = 0.10, (d) $x$ = 0.15 and (e) $x$ = 0.20.

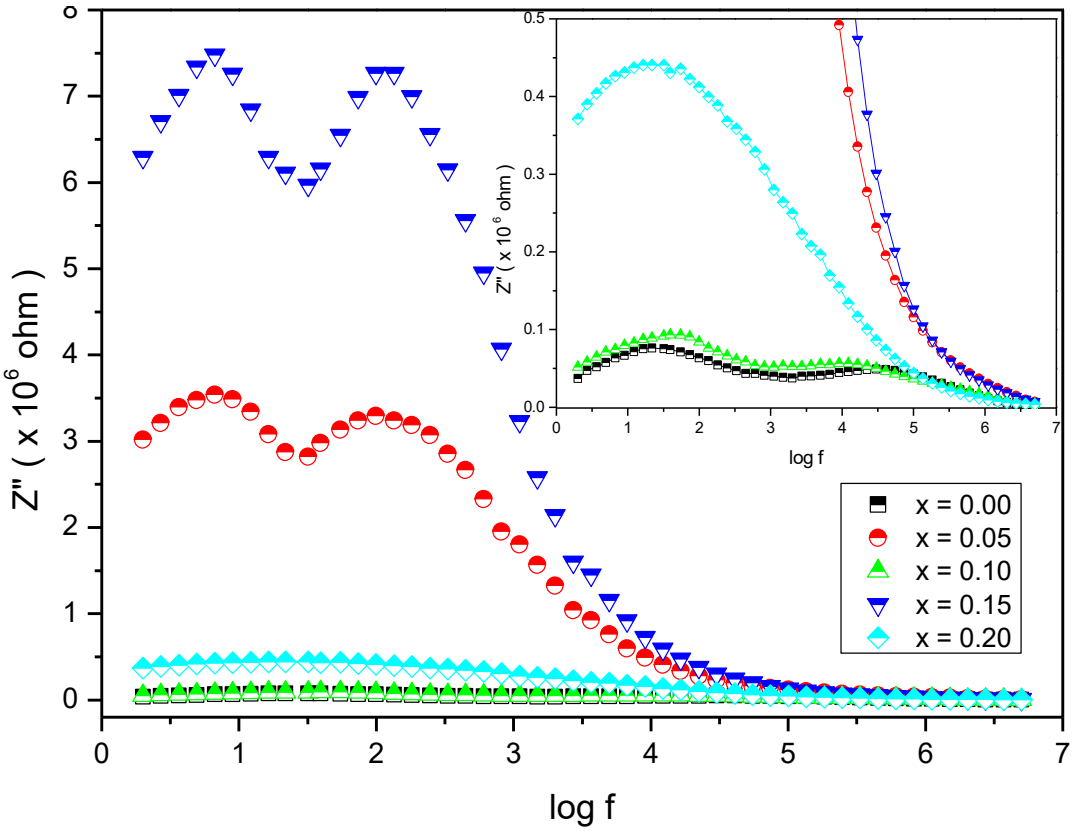


Figure 6.15: Variation of Z″ vs frequency at room temperature (308 K) for $Y_{2/3}Cu_3Ti_{4-x}Fe_xO_{12}$ ceramic ($x$ = 0.00, 0.05, 0.10, 0.15 and 0.20).

## 6.2.9 Modulus spectroscopic studies

The presence of long-range conduction phenomenon and different types of microscopic processes responsible for localized dielectric relaxations in $Y_{2/3}Cu_3Ti_{4-x}Fe_xO_{12}$ ($x$ = 0.10) ceramics were investigated separately by modulus studies. Impedance data was re-plotted in modulus formalism to confirm the presence of grain and grain boundary effects. But in this study, no such regular information was obtained by the Cole-Cole plot between M′ and M″ as shown in Fig. 6.16(a). The Cole–Cole plot in the modulus formalism justifies a poly-dispersive nature for the dielectric relaxation at low frequencies. Such observations may be related to the lack of resorting force governing the mobility of charge carriers under the action of an induced electric field. This behavior supports the long-range mobility of charge carriers.

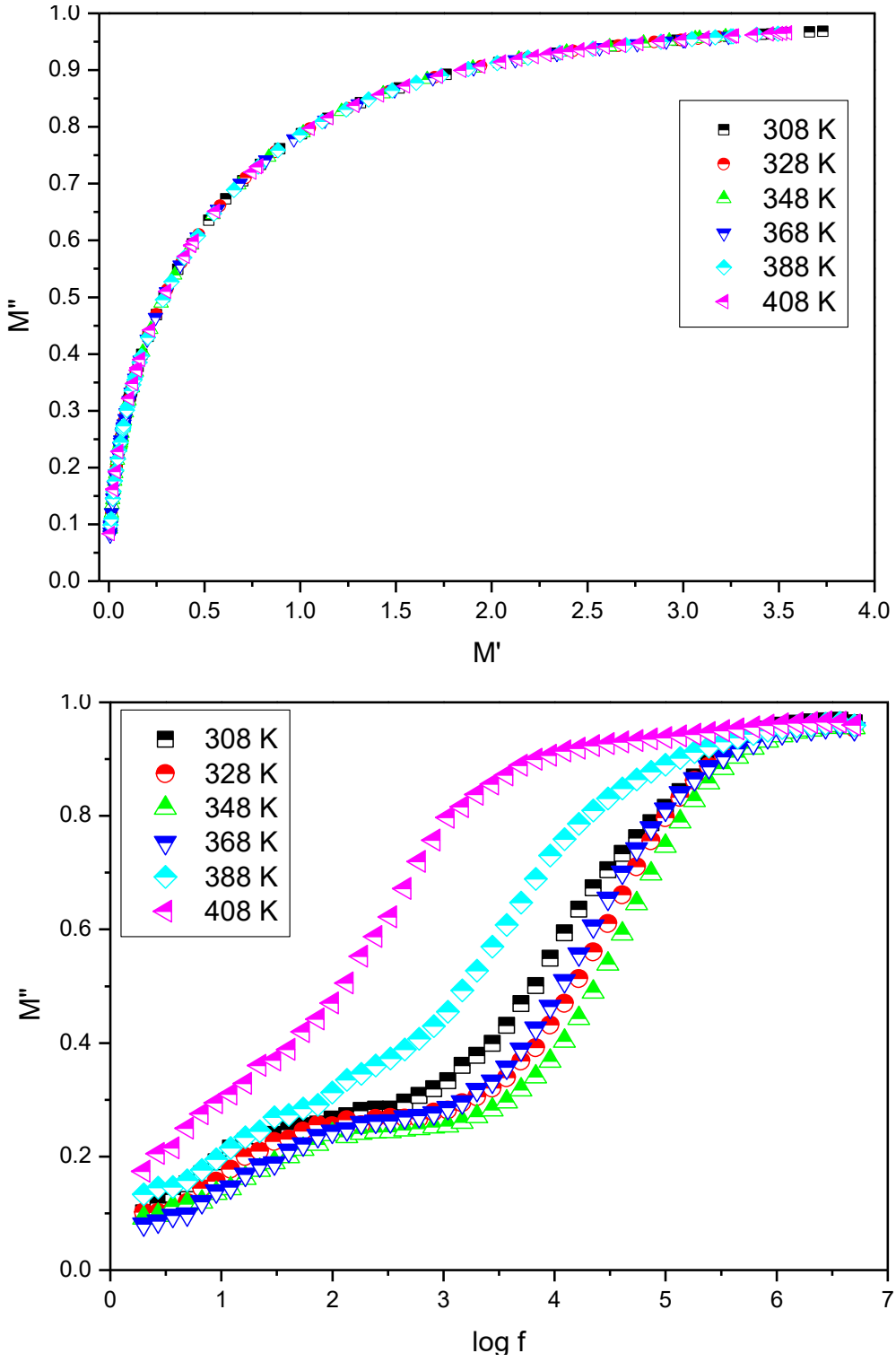


Figure 6.16: (a) Electric modulus plots (M′ vs M″) (b) Variation of M″ vs frequency at a few selected temperature for sintered $Y_{2/3}Cu_3Ti_{4-x}Fe_xO_{12}$ ($x$ = 0.10) ceramic.

In order to explain the modulus spectra of YCTFO ceramic, the variation of the imaginary part of electric modulus M″ is plotted against frequency at a few

selected temperatures and is shown in Fig. 6.16(b). It also confirms the presence of well-defined relaxation showing two types of relaxation peaks. The presence of relaxation peak in the higher frequency region may be due to grain boundary while lower frequency region may be due to electrode effects. These results also coincide with those of impedance results. The capacitance of grain boundary was calculated from the plot and recorded in Table 6.5. The values of capacitance were found to be nearly constant at a different temperature which was confirmed from the same peak height of the grain boundary with increasing temperature as shown in the M″ vs. log f plot (Fig. 6.16b). Further, the relaxation peaks shift to higher frequency region with increasing temperature and providing direct evidence for temperature dependent relaxation. This behavior also suggests that the dielectric relaxation is thermally activated (Mandal *et al.,* 2010).

## 6.2.10 Study of AC Conductivity

AC conductivity of mixed transition metal oxide ceramics is analogous to other ionic conductors. Variation of Ac conductivity ($\sigma_{ac}$) of ionic conductor as a function of frequency usually follows the relation:

$$\sigma_{ac} = \varepsilon\varepsilon_0\omega\tan\delta \qquad (6.2)$$

where $\omega = 2\pi f$ being the angular frequency *f*, $\varepsilon_0$ the permittivity of free space ($\varepsilon_0 = 8.854 \times 10^{-12}$ F/m), $\varepsilon$ is the relative dielectric constant (i.e. the real part) and tan $\delta$ is the dielectric loss of the ceramic. A detailed study of ac conductivity was carried out with variation of frequency and temperature from the resistance data obtained from LCR measurement. Frequency-dependent ac conduction mechanism in ceramic materials is usually explained in terms of Jonscher's Universal power law, which is applicable over a wide range of frequency and temperature. The law is expressed as follow:

$$\sigma_t(\omega) = \sigma_{dc}(T) + \sigma_{ac}(\omega,T) \qquad (6.3)$$

where $\sigma_t$ is the total conductivity and $\sigma_{dc}$ the dc conductivity i.e. the frequency independent part of ac conductivity which is basically due to electronic or dc contribution. However, $\sigma_{dc}$ is negligibly small compared to that of $\sigma_t$. Thus, $\sigma_t$ can be

considered to be due to $\sigma_{ac}(\omega)$. The frequency dependent part of AC conductivity is given by Jonscher's power law:

$$\sigma_{ac}(\omega) = A_1\omega_1^{s_1} + A_2\omega_2^{s_2} \qquad (6.4)$$

where $A_1$, and $A_2$ are constants and $\omega_1$, and $\omega_2$ are the angular frequencies ($\omega = 2\pi f$) of applied ac field, $s_1$, and $s_2$ are the frequency exponents. The constant 'A' determines the strength of polarizability while the constant 's' being the frequency exponent represents the degree of interaction between mobile ions and lattice around them. The variation of ac electrical conductivity as a function of frequency at different temperature for YCTFO (x = 0.10) ceramic is shown in Fig. 6.17 which indicates that the total conductivity, $\sigma_t(\omega)$, exhibits weak frequency dependence at low frequency, then it increases rapidly. It is also clear from Fig. 6.17 that the ac conductivity increases with increase in frequency indicating thereby the dispersion in conductivity due to frequency. Dispersion in conductivity gets narrower with the increase in temperature.

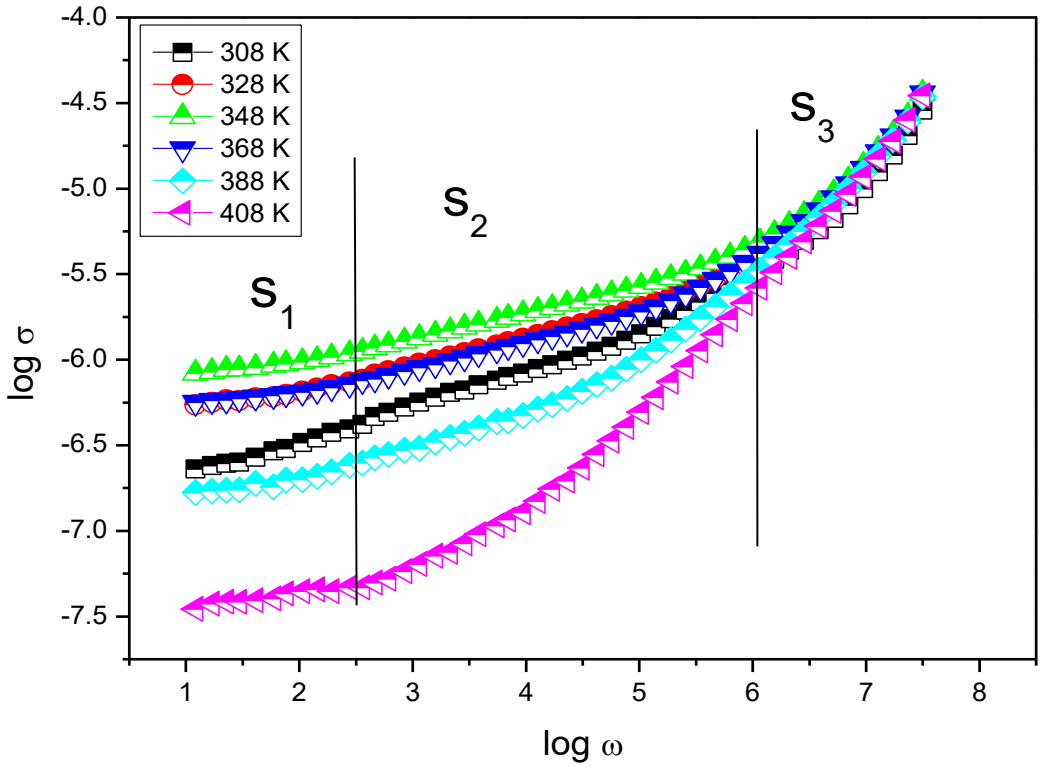


Figure 6.17: Variation of conductivity with frequency at a few selected temperatures for sintered $Y_{2/3}Cu_3Ti_{4-x}Fe_xO_{12}$ ($x$ = 0.10) ceramic.

The frequency exponential constant‘s’ is supposed to be solely due to material properties. It is clear from the above Eqn. 6.4 that the frequency exponent ‘s’ is also a function of temperature. It decreases with increase in temperature; however, the aforesaid equation is satisfied only at a lower temperature. The variation of exponent ‘s’ with temperature provides valuable information in an assignment of the predominant conduction mechanism of ac conductivity in any material. One can suggest the appropriate model for the conduction mechanism in the light of the different theoretical models correlating the conduction mechanism of ac conductivity with the variation of the exponent ‘s’ with temperature. In the literature, various models have been proposed to explain the behavior of the exponent ‘s’ such as small polaron tunneling (SPT), overlapping large-polaron tunneling (OLPT), quantum mechanical tunneling (QMT) and the correlated barrier hopping (CBH).

It is also reported in literature that the value of exponent ‘s’ is not always constant (Elliot, 1987). If it increases with temperature, small polaron tunneling is the predominant mechanism (Meaz *et al.*, 2003) while a minimum value of ‘s’ followed by an increase suggests that the conduction is predominantly due to overlapping large polaron tunneling mechanism (Ghosh 1990). If the value of ‘s’ remains temperature independent, quantum mechanical tunneling is the possibility (Austin 1969)). On the other hand the Correlated Barrier Hopping mechanism (Funke 1993, Dai *et al*., 1995) is usually associated with a decrease in the value of ‘s’ with temperature. CBH model primarily assumes that conduction occurs via a bipolaron hopping process where two polarons simultaneously hop over the potential barrier between two charged defect states $D^+$ and $D^-$ and that the barrier height is correlated with the inter-site separation via coulombic interaction. Further, Shimakawa (1981) suggested that at higher temperature, $D^0$ state is produced by thermal excitation of $D^+$ and $D^-$ states. A single polaron hopping process becomes the dominant process in which there is one electron hopping between $D^0$ and $D^+$ and hole between $D^0$ and $D^-$.

In fact, variation of ac conductivity with frequency is in association with displacement of carriers. These carriers move through randomly distributed localized sites with the limit of the sample by discrete hops. Information regarding frequency dependent part of ac conductivity can be obtained by analyzing the term $A\omega^s$, responsible for carrier conduction. The aforesaid distinct mechanisms for carrier

conduction are usually pronounced in ceramic materials. It is also clear from the Fig. 6.17 that the ac conductivity plot with frequency shows three different slops as divided by two vertical lines, first in the lower, second in the middle and third in the higher frequency region. In real practice, the frequency dependency of ac conductivity in ceramic materials doesn't bound to follow Jonscher's power law, the simpler only as discussed above; rather it follows a double power law which can be given as:

$$\sigma_t = \sigma_{dc} + A\omega^{s_1} + B\omega^{s_2} \qquad (6.5)$$

where $\sigma_t$ is the total conductivity, $\sigma_{dc}$ is the frequency independent part of ac conductivity, the exponent $s_1$ ($0 \leq s_1 \leq 1$) describes the low frequency region which is due to translational hopping of ions while the exponent $s_2$ ($0 \leq s_2 \leq 2$) signifies the high frequency region, indicating the existence of well-localized relaxation or re-orientational process the activation energy of which is mainly due to reorientation ionic hopping (Elliot, 1987, Funke, 1993). The values of $s_1$ and $s_2$ were calculated from Fig. 6.17, in low and high frequency regions, respectively which are listed in Table 6.6.

**Table 6.6:** Strength of polarizability (A & B) and frequency exponent ($s_1$ and $s_2$) of sintered $Y_{2/3}Cu_3Ti_{4-x}Fe_xO_{12}$ ($x$ = 0.10) ceramic.

| **Temperature ( in K)** | **A** | **$s_1$** | **B** | **$s_2$** |
|---|---|---|---|---|
| 308 | $1.949 \times 10^{-8}$ | 0.37018 | $1.55 \times 10^{-11}$ | 0.83145 |
| 328 | $1.028\times 10^{-7}$ | 0.25729 | $2.63 \times 10^{-11}$ | 0.81364 |
| 348 | $2.010\times 10^{-7}$ | 0.2234 | $6.89 \times 10^{-11}$ | 0.75942 |
| 368 | $5.799\times 10^{-8}$ | 0.30091 | $3.61 \times 10^{-11}$ | 0.79703 |
| 388 | $3.538\times 10^{-9}$ | 0.48718 | $2.86 \times 10^{-11}$ | 0.80782 |
| 408 | $1.575\times 10^{-10}$ | 0.69644 | $9.78 \times 10^{-12}$ | 0.87115 |

T

he variation of exponents with temperature is shown in Fig. 6.18. It is evident from the figure that the value of $s_1$ first decreases up to temperature 348 K and then increases while the value of $s_2$ remains almost constant.

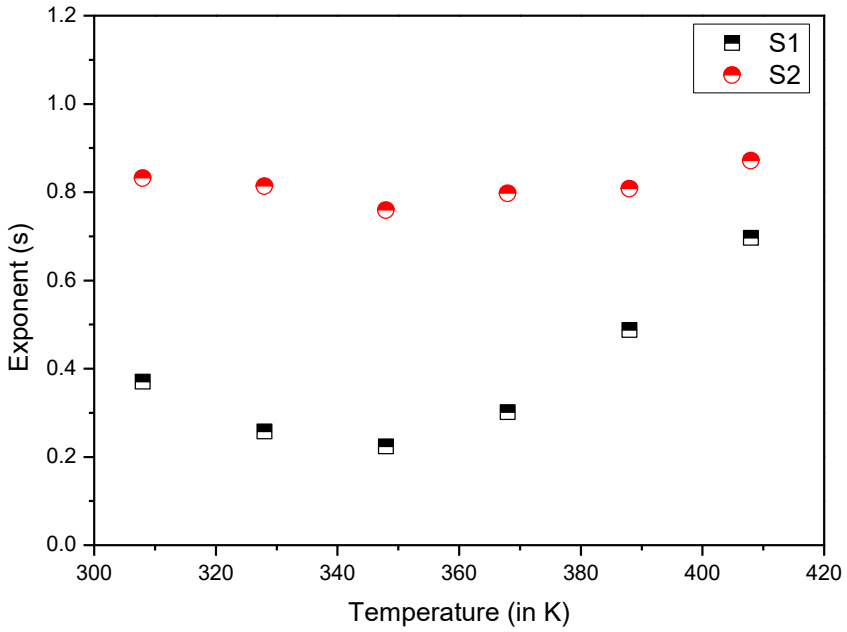


Figure 6.18: Variation of frequency exponents ($s_1$ and $s_2$) with temperature for sintered $Y_{2/3}Cu_3Ti_{4-x}Fe_xO_{12}$ ($x$ = 0.10) ceramic.

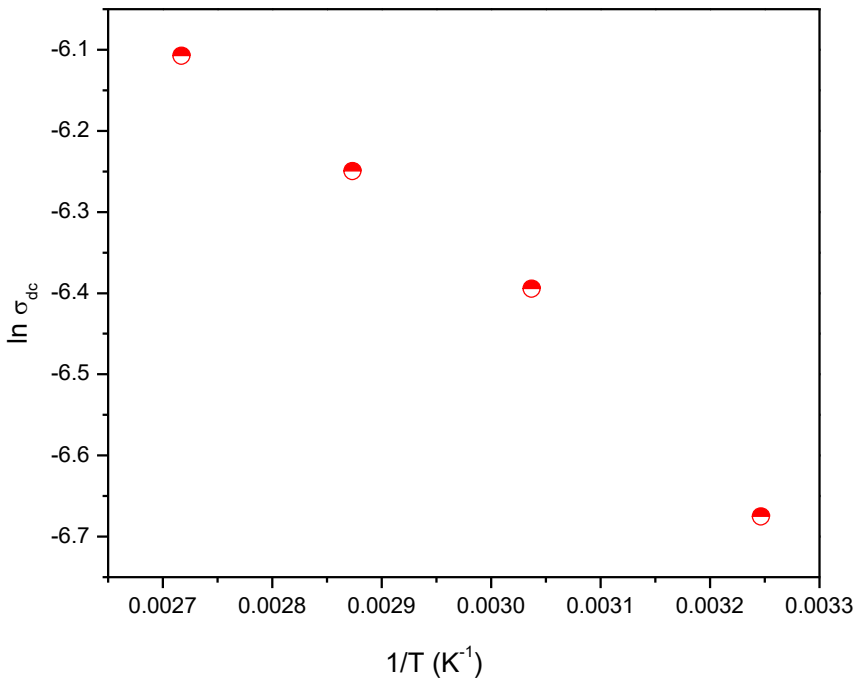


Figure 6.19: Plot of dc conductivity with inverse of temperature for sintered $Y_{2/3}Cu_3Ti_{4-x}Fe_xO_{12}$ ($x$ = 0.10) ceramic.

The hopping parameters $s_1$ and $s_2$ both assumes a maximum value ~0.70 and 0.87 at 408 K, respectively for YCTFO ceramic. Such behavior resembles with those of observations in case conductance due to large polaron tunneling process which suggests that the value of s decreases up to a certain temperature and then increases (Ghosh, 1990). It can be also deduced that the slopes $s_1$ and $s_2$ of Fig. 6.17 are corresponding to grain boundary and grain conductivity, respectively. However, Almond proposed that microstructural network in the system is responsible for this power law behavior (Almond et al., 2004). Hopping mechanism is extensively studied over a wide range of ceramics. The conductivity in the low frequency region is associated with successful hops. However, there may be a number of unsuccessful hops above and beyond the low frequency region. The change in the ratio of successful to unsuccessful hops causes a dispersive in conductivity.

An approximate value of dc conductivity of $Y_{2/3}Cu_3Ti_{4-x}Fe_xO_{12}$ ($x$ = 0.10) ceramic was also obtained from the Fig. 6.17. The temperature dependent variation of dc conductivity is expressed by Arrhenius equation as follows:

$$\sigma_{dc}(T) = \sigma_o.e^{-E/KT} \qquad (6.6)$$

where E is the activation energy of dc conduction. Fig. 6.19 shows the variation of ln $\sigma_{dc}$ with inverse of temperature. The activation energy for dc conductivity was found to be 0.091eV.

## 6.3 Conclusion

Nano-sized $Y_{2/3}Cu_3Ti_{4-x}Fe_xO_{12}$ ceramic ($x$ = 0.00, 0.05, 0.10, 0.15 and 0.20) was successfully synthesized by the semi-wet route using metal nitrate solution and solid $TiO_2$ powder in stoichiometric ratio. Single-phase formation of all the sintered ceramics was confirmed by XRD. Scanning electron micrographs shows bimodal non-uniform grain size distribution consisting of small smooth surfaced grains with some pores. Anomalous grain growth is observed in these samples. This is due to partial melting of CuO, which promotes anomalous grain growth. The dielectric property of all synthesized YCTFO ceramics is due to the combined effect of interfacial polarization and formation of barrier layer at grain and grain boundaries interface and their special heterogeneous microstructure. The impedance analysis shows two major contributions associated with the grains and the grain boundaries.